POLITECNICO DI TORINO

Master of Science in Mechanical Engineering

Analysis of cooling solutions in a gas turbine blade by means of CHT CFD

A.Y. 2018/2019

Supervisors

Prof.ssa Daniela Anna Misul

Prof. Mirko Baratta

Candidate

Nicola Rosafio

Contents

Abstract

In a modern gas turbine, up to about 20% of the main compressor flow is bled off to perform cooling and sealing of hot-section components. As the energy demand increased, the technology behind the gas turbine cooling system has developed, adopting new designs to enhance the performance of the machine. This work focuses on the analysis of rib-turbulated cooling channels, adopted in the first row blades of an industrial gas turbine engine. Rib-turbulated cooling channels paved their way in the last decades to substitute smooth channels. The implementation of turbulators has the main effect to enhance the heat transfer between the cooling fluid and the blade material. On the other hand, the pressure losses increase, corresponding to an increased pumping power to let the cooling air flow. The simulations were performed through a commercial software, namely STAR CCM+. The study has been mainly devoted to the comparison of three different configurations: standard smooth channels and two turbulated geometries. The three different geometries were compared both in terms of fluid-dynamic and thermal performance. It was found that, by adopting turbulated channels, an increase in the heat transfer coefficient is achieved. Halving the coolant mass flow rate comes at a price of a penalization of the heat flux of 25%.

Keywords: gas turbines, turbomachinery, fluid-dynamics, conjugate heat transfer

Chapter 1

Introduction

1.1 Firm Introduction

EthosEnergy is a provider of rotating equipment services, in the fields of power, oil & gas and industrial markets.
The company was born as a joint venture between John Wood Group PLC and Siemens AG. Wood Group GTS and Siemens' TurboCare business unit were joined into EthosEnergy Group.
The GTS division of Wood Group grew to be an independent provider of rotating equipment services and solutions for clients in the power and oil & gas markets.
The offered services included: power plant engineering, procurement and construction; facility operations and maintenance; repair and overhaul, optimization and upgrade of gas, steam turbines, pumps, compressors and other high-speed rotating equipment.
'Turbo Services Network' was established in 1998 and grew from here through various acquisitions before all businesses were re-branded under 'TurboCare' and established as a business unit within Siemens in 2006. The company provided comprehensive service solutions for rotating equipment (gas and steam turbines, generators, and compressors) manufactured by all major OEMs.

1.2 Gas Turbines

Gas turbines are rotating turbomachineries, widespread for power production or to provide thrust in the aeronautic field. For this reason, throughout the years, many improvements have been introduced to increase the efficiency and the performance of such systems.
The reference cycle of a gas turbine is the Brayton-Joule cycle.
The cycle comprises 4 transformations. With reference to Fig. 1.1, 1-2 is the compression of the air sucked by the compressor from the environment, 2-3 is the heat adduction in

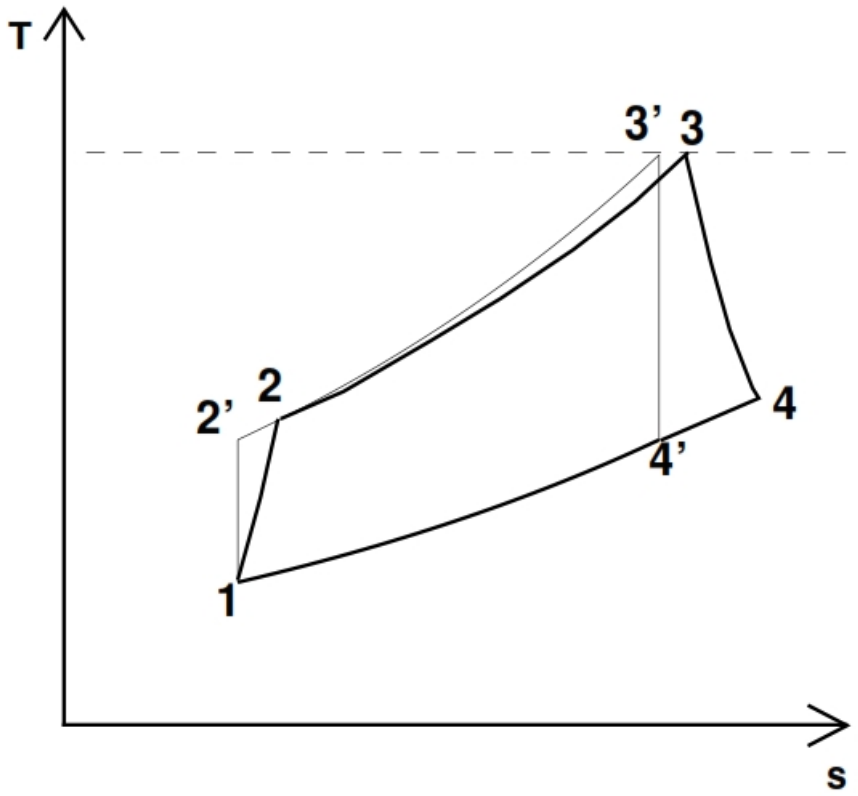

Figure 1.1: Brayton-Joule cycle
Real (continuous line), Ideal (dashed line)

the combustion chamber, 3-4 represents the expansion in the turbine, whereas the transformation 4-1 is the discharge of the exhaust gases in the environment. The temperature at point 3 is typically referred to as Turbine Inlet Temperature (TIT)
The net output of the plant comes from the difference between the work necessary for the compression and the one produced by the turbine.
Definig the compressor ratio as:

$$\beta_k = \frac{p_2}{p_1} \tag{1.1}$$

the efficiency of the ideal cycle is:

$$\eta_{id} = 1 - \frac{1}{\beta_k^{\frac{\gamma-1}{\gamma}}} \tag{1.2}$$

γ is the heat capacities ratio of the gas.
For a real cycle, the pressure loss in the combustor and the entropy generation in the compressor and in the turbine are taken into account. Some assumptions can still be made, since the mass flow rate of fuel is typically negligible with respect to the mass flow rate of the elaborated gas. For this reason, the properties of exhaust gases can be considered equal to the ones of the unburnt gas.

Neglecting the pneumatic efficiency of the burner, the real cycle efficiency is:

$$\eta_{cycle} = \left(1 - \frac{1}{\beta_k^{\frac{\gamma-1}{\gamma}}}\right)\left(\frac{\eta_t T_3 - \frac{T_{env}\beta_k^{\frac{\gamma-1}{\gamma}}}{\eta_k}}{T_3 - T_{env} - T_{env}\frac{\beta_k^{\frac{\gamma-1}{\gamma}}-1}{\eta_k}}\right) \tag{1.3}$$

The real efficiency depends mainly on T_3 and on β_k (Fig 1.2).

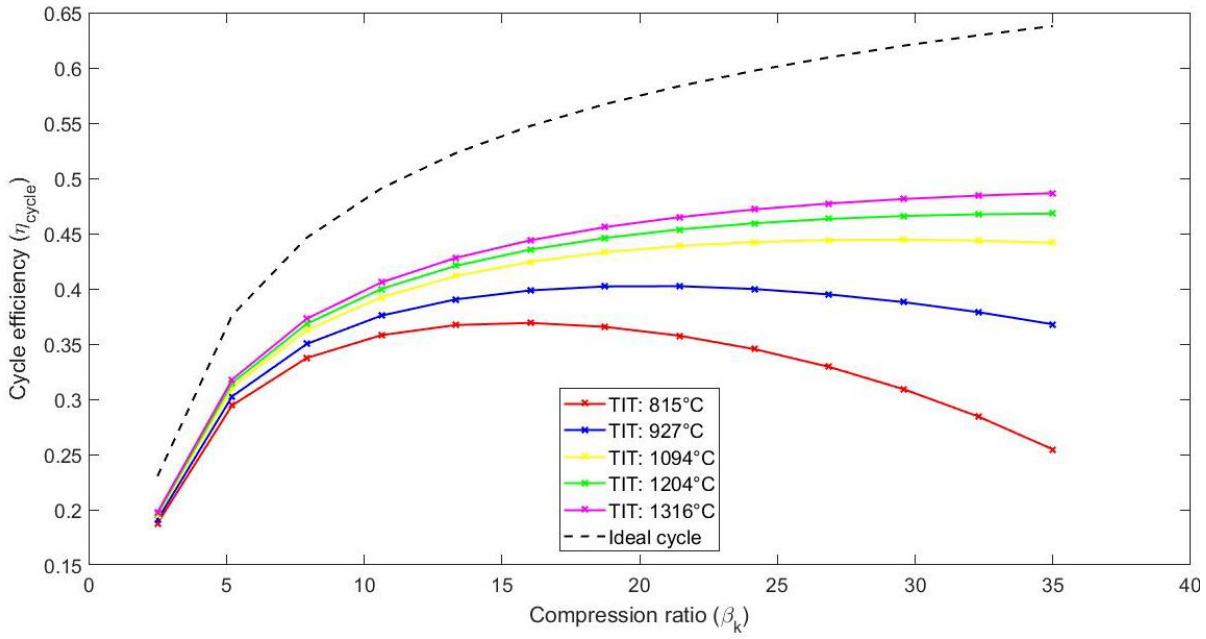

Figure 1.2: Real Cycle efficiency

In order to increase the efficiency of a gas plant β_k and T_3 are to be optimized, taking into account the operating limits of the machine. As far the compression ratio is concerned, the increase comes at the cost of dimensions of the machines (typically axial compressors provide a compression ratio equal to 1.2-1.3 per stage). Moreover, there is an optimal value depending on the TIT. On the other hand, an increase in TIT is always accompanied by an increase in the efficiency. In addition, a higher temperature at the end of the combustion is not linked to an increase in the dimensions of the plant. This is the reason why, the new studies focus on the increase of the TIT to boost both the power generation and the efficiency of the machine.

1.3 Gas Turbines-Cooling techniques

Over the years the threshold has been pushed, overcoming the melting temperatures of the blades' materials by far. Hence, the need to counterbalance the possible detrimental effect on the turbines' life duration has given birth to many minor modifications.

As a matter of fact, the thermodynamic cycle has remained unchanged, and the improvements regarded mainly the choice for highly performing materials, lower leakages and improvements of the cooling mechanism. To this end, part of the mass flow rate, elaborated in the compressor, is devoted to the cooling of the first stages of the turbine which suffer from large thermo-mechanical stresses due to the high values of both pressure and temperature. The cooling mechanisms are plenty: simply smooth cooling channels, rib-roughened cooling channels, impingement cooling and transpiration.

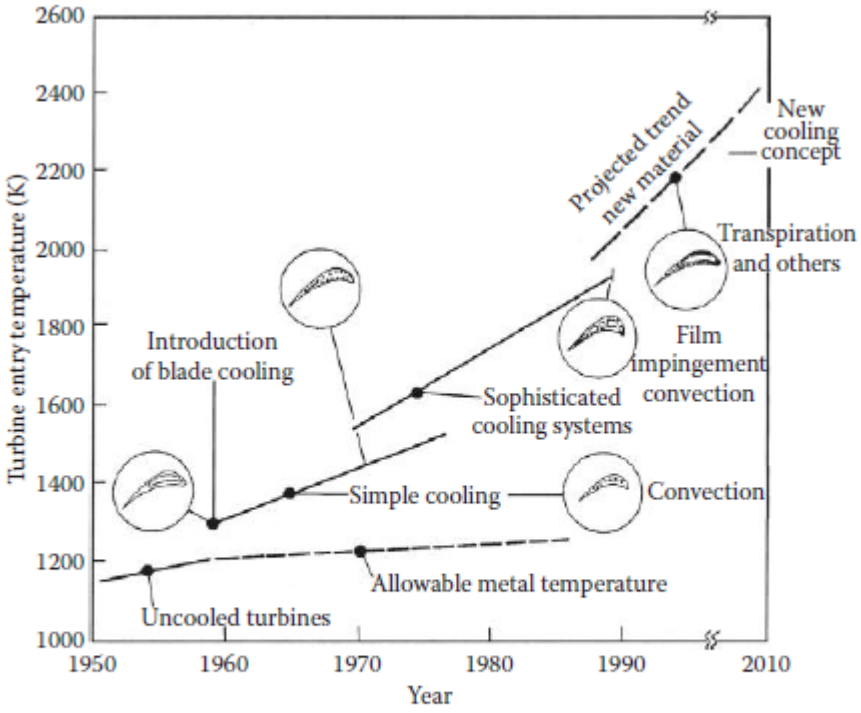

Figure 1.3: Evolution of TIT over the past years [1]

The study of the cooling performance has been subject of analysis for the last 50 years and the detailed description of these technologies is present in many studies. The analysis of cooling systems is of vital importance for the assessment of the engine performance. On one hand, the TIT threshold can be increased, far above the melting temperature of the blade material. On the other hand, the cold flow is extracted from the compressor, thus being compressed without being later expanded in the turbine, which turns out to be a loss of potential power generated.

For a land-based gas turbine, blades are cooled both internally and externally, which is the case of highly advanced machines. The internal cooling consists of letting a cold flow through the blade, which is achieved by cooling channels, pin-fin or jet-impingement cooling. The external cooling, on the other hand, consists of a protective film which shields the turbine blade from the hot gases in expansion. A comprehensive example of the cooling techniques is present in Fig. 1.4.

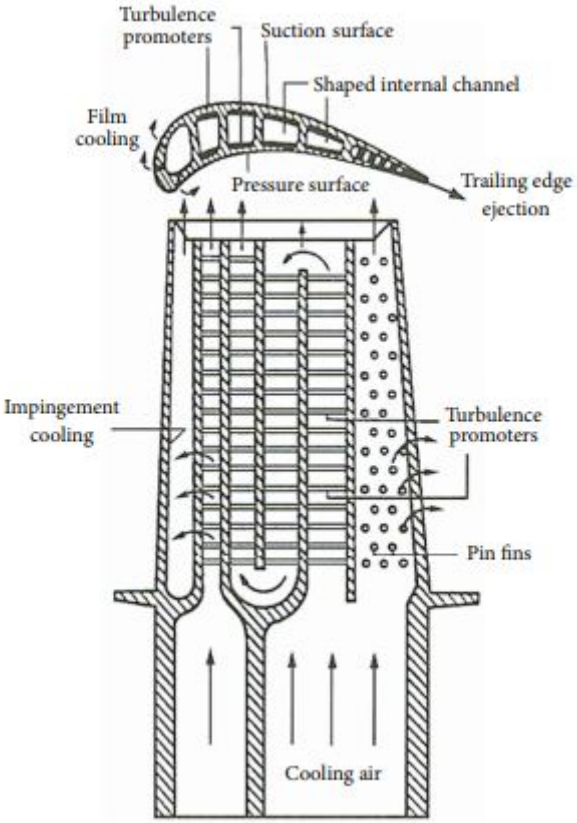

Figure 1.4: Gas Turbine - Blade cooling methods [2]

The jet-impingement cooling leads to the highest augmentation of the heat transfer performance, among all the cooling methods currently adopted. The main drawback of this solution is the inherent modification of the internal structure of the blade, and for this reason, it is typically adopted only where the thermal loads are large (leading edge). Simple cooling channels are instead adopted halfway between the leading edge and the trailing edge. The recent technology is to use turbulence-promoters such as ribs to improve the thermal performance of the cooling mechanism. As a matter of fact, turbulence enhances the diffusivity of the fluid, and creates separation zones which allow a better mixing of bulk cooling flow at low temperature and the near-wall flow which is heated by the blade. For these channels, the flow is radial, running from the blade root to the tip. There are 2 configurations which are currently widespread: the first one foresees a serpentine which allows for the reversal of the flow, whereas the second one consists of simple radial cooling channels. The former is preferrable especially when the cooling flow has not to be ejected from the blade tip and mixed with the expanded gas, e.g. when steam is used as a cooling flow.

Plenty of study has been spent concerning the geometry of the cooling channels (square, circular, rectangular) and of the ribs (spacing, shape, angle of attack).

Pin-fins are used in thin regions of the blade, where the implementation of the turbulated

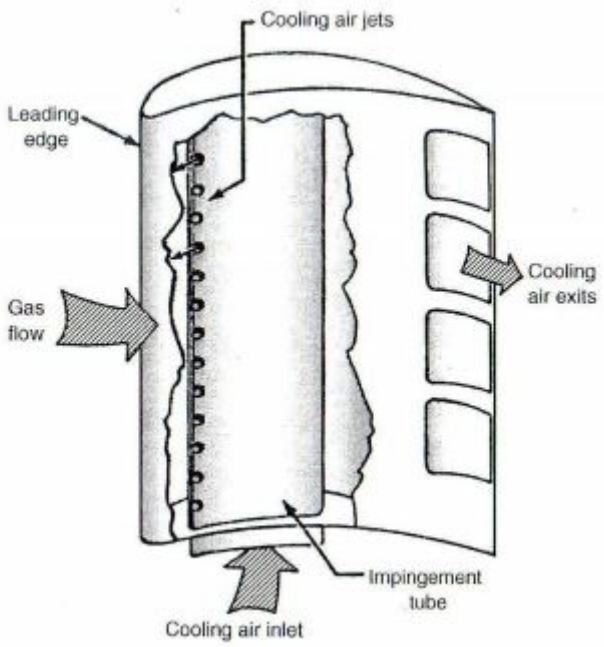

Figure 1.5: Jet Impingement Scheme [3]

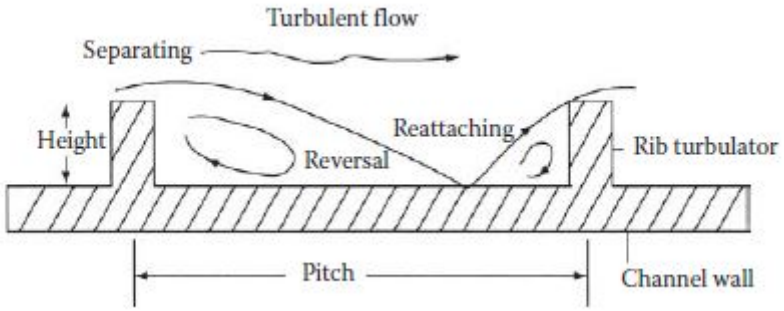

Figure 1.6: Flow schematic of Rib-Turbulated cooling channels

cooling channels might be impractical or even dangerous for the resistance of the blade. The heat transfer augmentation is achieved by protruding the hot surface into the main cooling flow. The effect is twofold. The available surface devoted to the heat transfer is increased, and in addition to this, the flow both upstream and downstream from pin is largely disturbed. The eventual outcome, is once again, an increased heat exchange. The study on this subject has been devoted to the evaluation of the effect of an array of fins, their shape, and 3D effect when the fin is does not cover the whole cross section of the cooling channel.

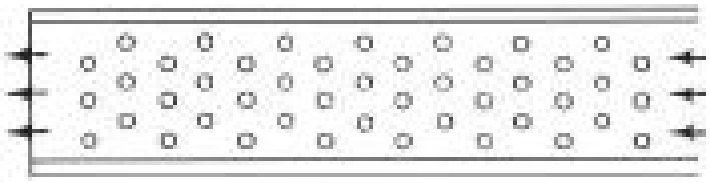

Figure 1.7: Pin-fin cooling technique

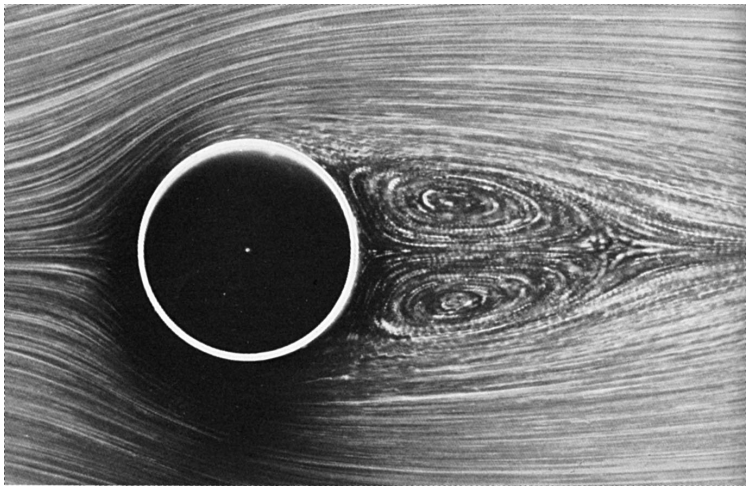

Figure 1.8: Flow past a cylinder

1.4 Machine description

The case of study is the TG20B7/8 produced by EthosEnergyGroup. The machine is characterized by an output of 48 MW, deriving from 19 stages of compression (15.4 is the total compression ratio) and 3 stages of expansion. Over the years the design of the machine has been revised in order to meet the performances of state-of-art turbines. The major modification of the machine concerns the inlet temperature of the turbine which has been augmented from 788^oC to 1129^oC.

For this reason a new design of the cooling mechanism has turned out to be necessary. Apart from thermal considerations, the old configuration also experienced operating issues. As a matter of fact, the cooling flow tendend to clog in the cooling inserts of the first vane of the machine. Consequently the statoric parts underwent an excessive heating, since, a reduced mass flow of coolant passed through the first vane of the machine. The main effect of this shortcoming in the cooling system is that the thermal loads were unsustainable for the vane, which deformed to a too high extent, and collided with the rotoric parts.

In the new confiuguration, the cooling mass flow rate is extracted from the combustor shell and sent to the first vane. The clogging issue is resolved, determining an increased reliability of the machine itself.

Also the inserts of the vane have been re-designed. The original configuration foresaw a single insert for the vane. Currently, 2 inserts are adopted, providing with impingement cooling on the leading edge and film cooling around the profile Fig. 1.9.

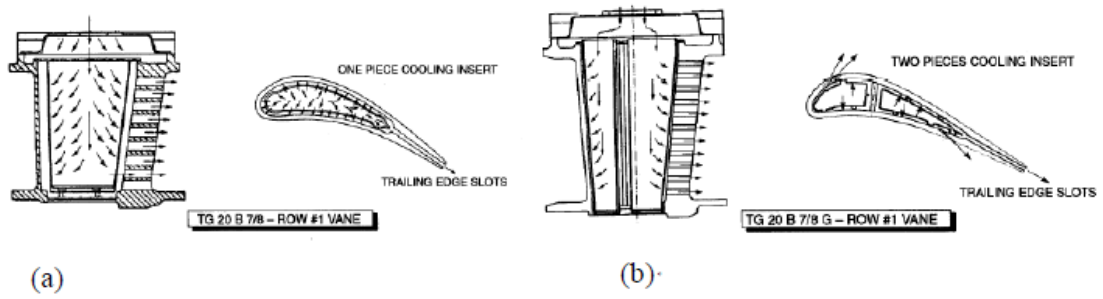

Figure 1.9: Row #1 Vane design updates
(a) Old design - (b) New design

As far as the Blade cooling technique is concerned, the original design was characterized by radial smooth channels which ran through the profile. The latter are manufactured via quartz rods during the casting process, which were later removed. The main drawback of this configuration is that the channels had a blend halfway from root to tip, which had many rods fracture when removed, thus damaging the blade and making it unusable. The scrap rate was as high as 70 %.
Despite the effort spent in changing the manufacturing process, a new configuraton seemed inevitable. The lower part of the cooling channels has been removed and substituted by an Anima which feeds the coolant up to the profile root. The manufacturing process is inherently more reliable, since the feature is obtained with a ceramic core easily removed after casting, in the place of the quartz rods which underwent rupture during removal.
The cooling mechanism is still under investigation and this work is devoted to its analysis.

Chapter 2

Theoretical Background

2.1 Governing equations

The complete description of a fluid motion needs 3 equations to be solved:

- **Continuity Equation**
- **Momentum Equation**
- **Energy Equation**

2.1.1 Continuity Equation

The continuity equation gives a mathematical substance to the mass conservation. The formulation is the following:

$$\frac{\partial \rho}{\partial t} + \boldsymbol{\nabla} \cdot (\rho \mathbf{u}) = 0 \tag{2.1}$$

where ρ is the density and $\mathbf{u}$ is the velocity.

2.1.2 Momentum Equation

The momentum equation is the following:

$$\frac{\partial (\rho \mathbf{u})}{\partial t} + \boldsymbol{\nabla} \cdot \rho \mathbf{u} \otimes \mathbf{u} + \nabla p = \boldsymbol{\nabla} \cdot \Pi_{\nu} + \rho \mathbf{a} \tag{2.2}$$

where Π_{ν} is the viscous stress tensor and $\rho \mathbf{a}$ is the momentum source or sink, deriving from the presence of external force fields.

2.1.3 Energy Equation

The energy equation is the following:

$$\frac{\partial \rho e_t}{\partial t} + \boldsymbol{\nabla} \cdot (\rho e_t \mathbf{u} + p\mathbf{u}) = \boldsymbol{\nabla} \cdot (\mathbf{q}_\alpha + \Pi_\nu \cdot \mathbf{u}) + \frac{\partial Q}{\partial t} \tag{2.3}$$

where e_t is the total specific energy, p is the pressure, $\mathbf{q}_\alpha$ is the specific thermal heat flux, $\Pi_\nu \cdot \mathbf{u}$ is the rate of work done by the viscous stresses and $\frac{\partial Q}{\partial t}$ is the rate of heat coming from external agents.
When the flow is incompressible, the energy equation can be solved after Continuity and Momentum equation. As a matter of fact, the density will not be affected by any other quantity, so that the velocity and pressure fields, will be almost independent from the Temperature.

2.1.4 Equation of State

In the complete set of equations we have 7 unknowns ($p, T, \boldsymbol{u}, e, \rho$), for 5 scalar equations. Thus, as above formulated, the problem is not closed. Two additional equations have to be introduced in the formulation of the problem. Namely, the material properties have to be linked with the thermodynamic state. A possible solution is to use p and T as independent variables and express the density and the specific energy as their functions:

$$\rho = \rho(p, T) \qquad e = e(p, T) \tag{2.4}$$

In our case we relied on the perfect gas model, for which:

$$p = \rho R T \qquad e = c_v T \qquad h = c_p T \tag{2.5}$$

Moreover we need to specify the values for the thermal conductivity and viscosity. In the case of a perfect gas the Sunderland equations can be adopted:

$$\mu = C_1 \frac{T^{\frac{3}{2}}}{T + C_2} \qquad k = C_3 \frac{T^{\frac{3}{2}}}{T + C_4} \tag{2.6}$$

where the constants C_{1-4} are given for a certain gas.
Whenever the perfect gas model is not a viable option, the relations between the thermodynamic variables can be found in the form of tables or charts.

2.2 Turbulence Modelling

The occurrence of turbulence motion is mainly related to the Reynold's number which characterizes the flow. In particular, when Reynold's number overcomes a certain threshold, the organized motion which characterizes a laminar flow turns into a chaotic one. The instability arises when the inertial forces overcome the viscous forces which, from a phenomenological point of view, manifests itself in the form of of different length-scales eddies along the flow.
Turbulence is a 3D, time-dependent phenomenon. For this reason the amount of information required to completely describe the motion is plentiful.

2.2.1 Closure Problem-RANS equations

Theoretically speaking all the information necessary to solve for a turbulent flow, are already present in the Navier-Stokes equations. Indeed the eddies' length-scales are order of magnitudes higher than molecular distances. Despite this, the presence of random fluctuations requires the adoption of a statistical approach to solve for the quantities of interest.
Reynolds proposed an averaged version of the NS equations, which accounted for the fluctuating quantities by means of an averaging procedure.
As fas as averaging is concerned, 3 types can be discussed: **spatial average**, **time average**, **ensembling average**. For turbulence modelling, it is assumed that these 3 procedures yield the same result: we assume that turbulence is an **ergodic process**. Since in most practical cases, turbulent flows are inhomogeneous, the most appropriate form of averaging is the **time average** [4].
The time average of a quantity $f(\mathbf{x}, t)$ is defined as follows:

$$F_T(\mathbf{x}) = \lim_{t\to\infty} \frac{1}{T} \int_t^{t+T} f(\mathbf{x}, t) dt \tag{2.7}$$

This is applied to randomly behaving quantities which can be written in the form:

$$\phi(\mathbf{x}, t) = \overline{\phi}(\mathbf{x}, t) + \phi'(\mathbf{x}, t) \tag{2.8}$$

where $\overline{\phi}(\mathbf{x}, t)$ is the mean value and $\phi'(\mathbf{x}, t)$ is the fluctuating contribution.
When we apply the time averaging to such quantities, we have that:

$$\overline{\phi}(\mathbf{x}, t) = \lim_{t\to\infty} \frac{1}{T} \int_t^{t+T} \phi(\mathbf{x}, t) dt \tag{2.9}$$

$$\lim_{t\to\infty}\frac{1}{T}\int_{t}^{t+T}\phi'(\mathbf{x},t)dt=0 \tag{2.10}$$

As far as NSF equations are concerned, the presence of non-linear terms gives birth to new contributions. As a matter of fact, when averaging linear terms (since derivative and definite integrals are linear), we only need to substitute the initial quantity with the average one. For non linear terms, like the momentum advection, we have:

$$\overline{\phi\Psi}=\overline{\phi}\ \overline{\Psi}+\phi'\Psi' \tag{2.11}$$

Neglecting the potential energy along with the generation term, and then introducing the enthalpy, the Reynolds averaged NSF equations for an incompressible flow are the following:

$$\boldsymbol{\nabla}\cdot\overline{\mathbf{u}}=0 \tag{2.12}$$

$$\rho\frac{\partial(\overline{\mathbf{u}})}{\partial t}+\rho\boldsymbol{\nabla}\cdot(\overline{\mathbf{u}}\otimes\overline{\mathbf{u}}+\overline{\mathbf{u}'}\otimes\overline{\mathbf{u}'})+\nabla\overline{p}=\boldsymbol{\nabla}\cdot\overline{\Pi}_{\nu}+\rho\overline{\mathbf{a}} \tag{2.13}$$

$$\rho\frac{\partial\overline{h}}{\partial t}+\rho\boldsymbol{\nabla}\cdot(\overline{h}\ \overline{\mathbf{u}}+h'\mathbf{u}'-k\nabla\overline{T})=\frac{\partial\overline{p}}{\partial t}+\boldsymbol{\nabla}\cdot(\overline{\Pi}_{\nu}\cdot\overline{\mathbf{u}}) \tag{2.14}$$

The term $\rho\boldsymbol{\nabla}\cdot(\overline{\mathbf{u}'}\otimes\overline{\mathbf{u}'})$ is typically referred to as **Reynolds stress tensor**. It is evident how the averaging procedure introduces new terms in the NSF system of equations. Arising from the non-linearities, the latter have the main drawback of increasing the number of unknowns we have to solve for. For this reason, the introduction of equations of state is not sufficient to close the system. To overcome these issues, many models have been developed to account for the turbulent quantities. The simplest models are called Algebraic, since the evaluation of turbulence, and mainly of the Reynold's stress tensor is performed by means of a scalar quantity. The most accurate model is the Large Eddy Simulation **LES**, in which the large eddies are simulated, whereas the small eddies are modelled. Even a complete solution of turbulent NSF is viable (**Direct Numerical Simulation**), but it is very demanding from a computational point of view.
In this work we will mainly concentrate on a 2-equation model which close the system by introducing 2 transport equations for the turbulent quantities: $\boldsymbol{k}$ and $\boldsymbol{w}$.

2.2.2 *k-w* model-SST modification

The model arises from the introduction of the kinetic energy of the fluctuations per unit mass: $\boldsymbol{k}$. It is often referred to as turbulent kinetic energy and it is the characteristic velocity of turbulence. The second quantity $\boldsymbol{w}$ is the dissipation per unit turbulence

kinetic energy. The canonical ***k-w*** model is the following:

$$\rho\frac{\partial k}{\partial t}+\rho\overline{u}_i\frac{\partial k}{\partial x_j}=\tau_{ij}\frac{\partial \overline{u}_i}{\partial x_j}-\beta^*\rho k w+\frac{\partial}{\partial x_j}\left[(\mu+\sigma^*\mu_T)\frac{\partial k}{\partial x_j}\right] \tag{2.15}$$

$$\rho\frac{\partial \omega}{\partial t}+\rho\overline{u}_j\frac{\partial \omega}{\partial x_j}=-\beta\rho\omega^2+\frac{\partial}{\partial x_j}\left[\sigma\mu_T\frac{\partial \omega}{\partial x_j}\right] \tag{2.16}$$

The ***k-w*** model has undergone major modifications over the decades in order to suitably predict experimental results in different conditions [4]. In our case, we will mainly concentrate on the **SST** modification. The modified equations are the following:

$$\rho\frac{\partial k}{\partial t}+\rho\overline{u}_i\frac{\partial k}{\partial x_j}=P_k-\beta^*\rho k w+\frac{\partial}{\partial x_j}\left[(\mu+\sigma^*\mu_T)\frac{\partial k}{\partial x_j}\right] \tag{2.17}$$

$$\rho\frac{\partial \omega}{\partial t}+\rho\overline{u}_j\frac{\partial \omega}{\partial x_j}=\rho\alpha S^2-\beta\rho\omega^2+\frac{\partial}{\partial x_j}\left[(\mu+\sigma_\omega\mu_T)\frac{\partial \omega}{\partial x_j}\right]+2(1-F_1)\sigma_{\omega 2}\frac{1}{\omega}\frac{\partial k}{\partial x_i}\frac{\partial \omega}{\partial x_i} \tag{2.18}$$

The main advantage of this modification is that the model combines the achievements of both the ***k-w*** and the ***k-*** $\boldsymbol{\epsilon}$ models. As a matter of fact it can be used to model turbulence all the way down to the viscous sub-layer (***k-w***) and the and closely represents regions close to free-surfaces (***k-*** $\boldsymbol{\epsilon}$).

2.3 Finite Volume Method

NSF equations can be solved analytically only in very few cases, under particular conditions. For most practical problems, we need to resort to a numerical approach to find an approximated solution to these equations.
The starting point of the numerical approach is the partition of the domain into elements, forming the mesh. Then the discretized version of the equations is obtained through different approaches, like Finite Elements Method or Finite Difference Method.
Most CFD commercial code adopt the Finite Volume Method (FVM). As a start, an integral formulation of the equations is formulated, which is later turned into the discretized version. The main advantage of FVM is that it is conservative by construction, in the sense that, even though variables may be discontinuous, momentum and energy are conserved. Moreover, the method is the most suitable when unstructured mesh are adopted in fluid-dynamics.
Consider the general transport equation of a scalar quantity:

$$\frac{\partial(\rho\Phi)}{\partial t}+\boldsymbol{\nabla}\cdot(\rho\mathbf{u}\Phi)=\boldsymbol{\nabla}\cdot(\Gamma\ \nabla(\Phi))+S_\Phi \tag{2.19}$$

The integral version of the equation is:

$$\int_{CV}\left(\int_t^{t+\Delta t}\frac{\partial(\rho\Phi)}{\partial t}dt\right)dV+\int_t^{t+\Delta t}\left(\int_A \mathbf{n}\cdot(\rho\mathbf{u}\Phi)dA\right)dt= \\ =\int_t^{t+\Delta t}\left(\int_A \mathbf{n}\cdot\Gamma\ \nabla(\Phi)dA\right)dt+\int_t^{t+\Delta t}\int_{CV}S_\Phi dVdt \tag{2.20}$$

In this integral formulation of the problem, the integrals must be evaluated in such a manner that a discretized version in obtained.
To this end, the actual Control Volume is subdived into smaller ones over which the integrals are computed. Fig. 2.1 shows an example for a computational grid typically adopted in the FVM.
The nodal points, at the centers of the control volumes are usually indicated in capital letters, whereas the interfaces are typically indicated with small letters. For the evaluation of integrals, referring to an orthogonal grid, the following approximations are made:

$$\int_{CV}\Phi dV=\overline{\Phi}_V*\Delta V \qquad \int_A\Phi dA=\overline{\Phi}_A*A \tag{2.21}$$

where $\overline{\Phi}_V$ and $\overline{\Phi}_A$ are the average values of Φ respectively over the volume and the interface of the computational cell.
In the case of FVM the unknowns of the discretized set of equations are the nodal Values of the quantities (namely Φ_V), thus also the surface averaged quantities have to be computed resorting to the volume averaged ones. For this reason it is necessary to adopt an approximate distribution of the quantities in between the nodal points. There are many possibilities to evaluate quantities at the interface, and here we report some.

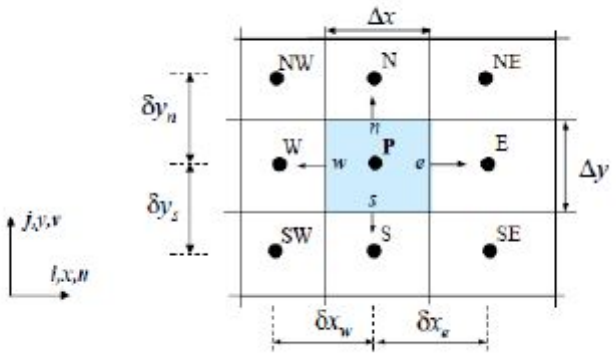

Figure 2.1: Computational grid

2.3.1 Central Differencing Scheme

As a start an introduction of the main properties of a differencing scheme is necessary:

- **Boundedness**
- **Transportiveness**
- **Conservativeness**
- **Accuracy**

Conservativeness of a differencing scheme means that the flux entering a CV through a boundary is equal to the flux exiting the neighbouring CV through the same boundary. For inconsistent representations, this property is not satisfied.
Boundedness of a differencing scheme yields that in absence of sources, the nodal value must be bounded by the boundary values.
Transportiveness refers to the ability of the differencing scheme to account for the directionality of the flow, particularly important when convective terms outweigh diffusion terms.
Accuracy is related to the errorr committed by estimating derivatives through nodal values.
In a central differencing scheme, the interface value of a quantity is obtained as the average of the nodal values at the CV sharing that interface, namely:

$$\Phi_e = \frac{\Phi_P + \Phi_E}{2} \tag{2.22}$$

As far as accuracy is concerned, the CDS is second-order accurate. Although conservative, the central differencing scheme is not trasportative and in the case of higly convective flows it is not bounded. The weight of convection with respect to diffusion is assessed by means of the Peclet number:

$$Pe = \frac{\rho u}{k\delta x} = \frac{F}{D} \tag{2.23}$$

where δx is the characteristic length of the cell. Whenerver $|Pe|>2$ the CDS is unbounded. An example is shown in Fig. 2.2 and Fig. 2.3 [5].

2.3.2 Upwind Differencing Scheme

The Upwind Differencing Scheme (UPS) accounts for flow direction to evaluate interface values. Namely:

$$\begin{aligned} \Phi_w &= \Phi_W \qquad when \;\; u > 0 \\ \Phi_w &= \Phi_P \qquad when \;\; u < 0 \end{aligned} \tag{2.24}$$

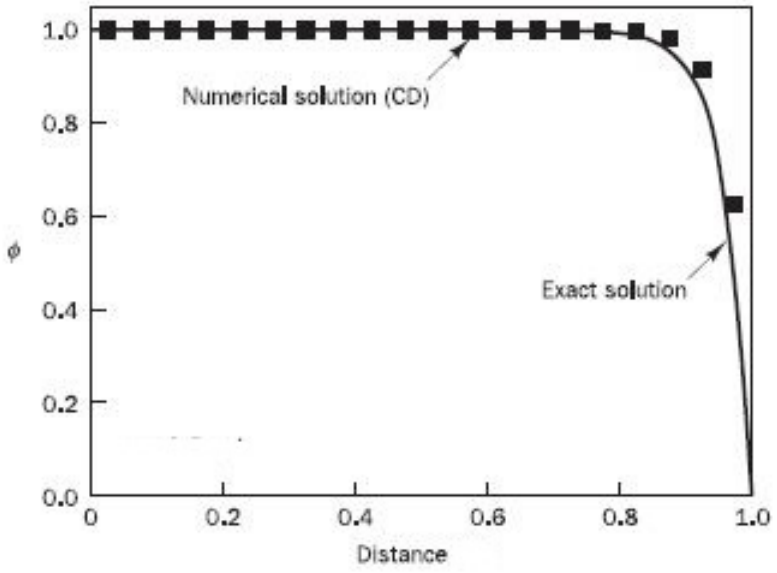

Figure 2.2: CDS - Pe=1.25

The UPS is bounded, transportative and conservative. Despite this the accuracy is first-order. The first order accuracy turns into the so called numerical diffusion, namely a diffusive term arising from the numerical discretization. This is overcome at the price of a finer grid, as shown in Fig. 2.4

2.3.3 Hybrid Differencing Scheme

The Hybrid Differencing scheme (HDS) is a mixture of the UDS and the CDS. Namely:

$$\begin{aligned} q_w &= F_w \left[\frac{1}{2} \left(1 + \frac{2}{Pe_w} \right) \Phi_W + \frac{1}{2} \left(1 - \frac{2}{Pe_w} \right) \Phi_P \right] \quad for -2 \leq Pe \leq 2 \\ q_w &= F_w \Phi_w \quad for \;\; Pe_w \geq 2 \\ q_w &= F_w \Phi_P \quad for \;\; Pe_w \leq -2 \end{aligned} \tag{2.25}$$

The HDS recovers the UPS whenever the Peclet number is ≥ 2, whereas it modifies the CDS in order to account for the flow direction when the Peclet number is ≤ 2. This scheme is conservative and unconditionally bounded, but, once again, it is first order accurate.

2.3.4 Explicit Euler Scheme

So far, only the spatial discretization has been considered, and a consistent time discretization for the time derivatives is necessary. The simpler scheme is the Explicit Euler

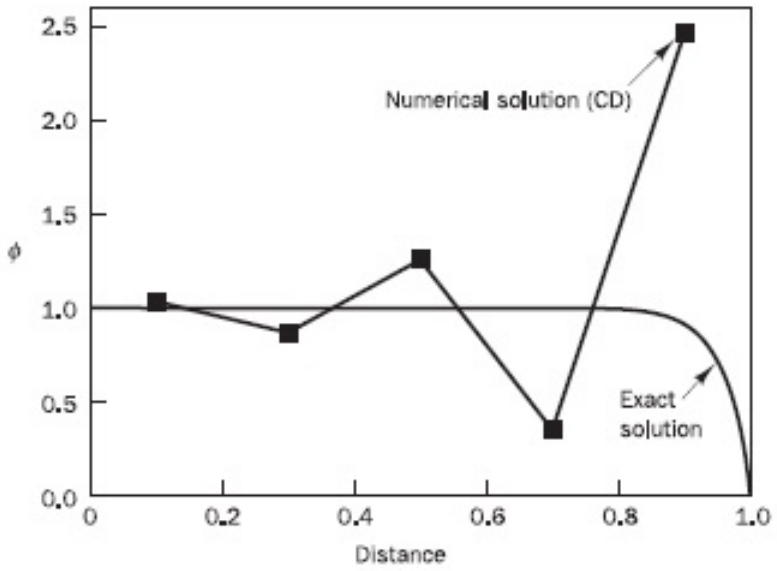

Figure 2.3: CDS - Pe=5

Scheme, (EES) namely:

$$\int_{CV}\left(\int_{t}^{t+\Delta t}\frac{\partial(\rho\Phi)}{\partial t}dt\right)dV=\rho(\Phi-\Phi^{0})\Delta V \tag{2.26}$$

where Φ is the quantity evaluated at the time $t+\Delta t$ and Φ^0 is evaluated at the time t. EES corresponds to a backward substitution of the time derivative with a time step equal to Δt. This discretization is said to be explicit because, after discretization, the resulting equation will be of the type:

$$a_P T_P = a_W T_W^0 + a_E T_E^0 + [a_P^0 - (a_W + a_E - S_P)]T_P^0 + S_u \tag{2.27}$$

and all the terms on the RHS are evaluated at the previous time instant.
Adopting a backward ratio, the EES is first order accurate in time. Despite being very easy, this scheme has some drawbacks. As a matter of fact, in order to have a bounded solution in time, it is necessary that:

$$\Delta t < \rho c\frac{(\Delta x)^2}{2k} \tag{2.28}$$

This restricts the possible choices of the time step. Moreover, the latter depends on the square of the spatial step, thus making this scheme very demanding when an improved spatial accuracy is sought.

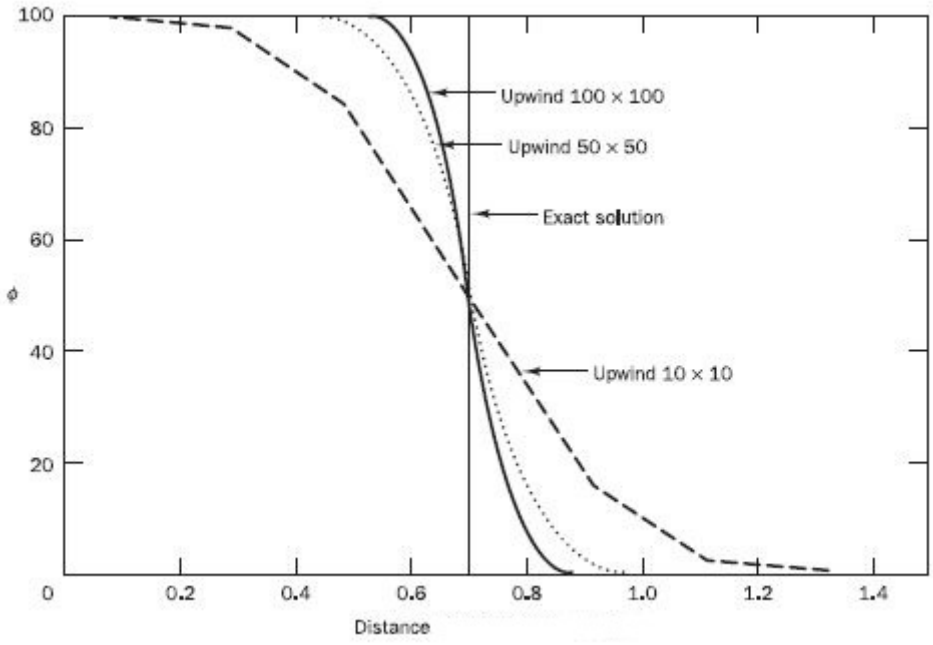

Figure 2.4: Numerical Diffusion

In general a time discretization can be written in the form:

$$\int_t^{t+\Delta t} T_P dt = [\Theta T_P + (1-\Theta)T_p^0]\Delta t \tag{2.29}$$

where the value of Θ defines the scheme itself. The EES is obtained for Θ=0;

2.3.5 Implicit Euler Scheme

A fully implicit scheme is obtained by setting Θ equal to 1. The discretized equations will be rearranged in the following manner:

$$a_P T_P = a_W T_W + a_E T_E + a_P^0 T_P^0 + S_u \tag{2.30}$$

In this case, we have the presence of the Temperature on both sides of the equatio, and a system of linear equation has to be solved at each time step.
The IES is unconditionally stable for any time step, and is, like EES, first order accurate in time.

2.3.6 Richardson's extrapolation - Grid Convergence Index

When adopting a discretization technique to solve complex equations, the Richardson's extrapolation provides a way to eliminate the Leading Order Error. For this reason it is convenient to estimate the continuum value (numerical solution for an extremely

fine mesh) with a higher order of accuracy. Considering the solutions obtained for 2 different grids, the hypothesis upon which the procedure is based is that the error dicreases monotonically as the mesh is refined [6]
Considering the numerical solution f, we can suppose that:

$$f = f_{exact} + g_1 h + g_2 h^2 + g_3 h^3 ... \tag{2.31}$$

where f_{exact} is the exact solution to the equations and $g_i h$ are error terms depending on the grid size h.
For a grid spacing ration $r = \frac{h_1}{h_2} = 2$, the following holds:

$$f_{exact} = \frac{4}{3} f_1 - \frac{1}{3} f_2 \tag{2.32}$$

where f_1 is the solution obtained for a fine grid and f_2 is the solution obtained for a coarser grid. Generalizing the procedure, we can write that:

$$f_{exact} = f_1 + \frac{f_1 - f_2}{r^p - 1} \tag{2.33}$$

p can be computed using 3 different mesh sizes as:

$$p = \frac{log(f_2 - f_4) - log(f_1 - f_2)}{log(r)} \tag{2.34}$$

The Richardson's extrapolation is not valid where discontinuities occurr, but it is helpful for the evaluation of integral quantities.
The Grid Convergence Index is used to estimate the error band of the solution, with respect to the numerical asymptotical solution, obtained for a very fine grid. Despite this, the numerical asymptotical solution may even disagree with the true solution of the problem, tough.
The GCI can be adopted even for refinement of the time discretization, instead of the spatial discretization. The CGI is defined as:

$$CGI_{fine} = \frac{F_s |\epsilon_r|}{(r^p - 1)} \tag{2.35}$$

where F_s is a safety factor (a recommended value is 1.25 for analysis involving 3 or more different grids).
For an analysis of a coarser grid, the relative error will be magnified according to the

order of convergence and the following relation holds:

$$CGI_{coarse} = \frac{F_s|\epsilon_r|r^p}{(r^p - 1)} \tag{2.36}$$

Once the grid has been chosen according to the level of numerical accuracy that one wants to reach, it is necessary to assure that our solution is in the asymptotic range of convergence. Whenever this occurs, the more the mesh is fine the more the result is numerically accurate.
The verification is simple:

$$GCI_{23} \simeq r^p CGI_{12} \tag{2.37}$$

2.3.7 Solving Procedure

The solution of the new set of discretized equations requires a convenient method, to converge as fast as possible. Two different approaches are adopted, depending on the case of study:

- Segregated Flow Solver
- Coupled Flow Solver

In the SFS the momentum equations of mass and momentum are solved one after the other. The main difficulty lies in the coupling of mass and momentum equations through velocity and pressure, whose gradient is the main momentum source. An appropriate algorythm (SIMPLE or PISO) is used to solve pressure-correction equation which satisfies the mass conservation equation. The pressure-correction equation is obtained by coupling mass and momentum equation.
The SFS was firstly used for incompressible flows. However it can withstand weakly compressible flows and natural convection problems characterized by low Rayleigh number. When either the Rayleigh number and Mach number are high or shock-waves have to be captured, the CFS is preferrable.
In order to solve the coupling, the mass conservation equation is rewritten in the form:

$$\sum_f \dot{m}_f = \sum_f (\dot{m}_f^* + \dot{m}_f\prime) = 0 \tag{2.38}$$

where:

- $\dot{m}_f^*$ is the uncorrected mass flux through a face of the cell
- $\dot{m}_f\prime$ is the mass flux correction which is obtained from the solution of the discretized momentum equation

The CFS features a simultaneous solution of the governing equations, meaning that they are treated as a vector of equations. In this case the velocity field is obtained from the momentum equation, then the pressure is calculated and the density is obtained from the equation of state.
The governing system of equations is treated in the following manner:

$$\frac{\partial}{\partial t}\int_V \mathbf{W}dV + \oint [\mathbf{F}-\mathbf{G}]\cdot\mathbf{a} = \int_V \mathbf{H}dV \tag{2.39}$$

where the vectors are:

$$\mathbf{W}=\begin{bmatrix}\rho\\ \rho\mathbf{v}\\ \rho E\end{bmatrix}\ \mathbf{F}=\begin{bmatrix}\rho\mathbf{v}\\ \rho\mathbf{v}\mathbf{v}+p\mathbf{I}\\ \rho\mathbf{v}H+p\mathbf{v}\end{bmatrix}\ \mathbf{G}=\begin{bmatrix}0\\ \mathbf{T}\\ \mathbf{T}\ \cdot\ \mathbf{v}+\dot{q}''\end{bmatrix}\ \mathbf{H}=\begin{bmatrix}S_u\\ \mathbf{f}_r+\mathbf{f}_g+\mathbf{f}_p+\mathbf{f}_u+\mathbf{f}_\omega+\mathbf{f}_L\\ S_u\end{bmatrix} \tag{2.40}$$

When the flow is incompressible, due to the numerical structure, convergence problems may arise and preconditioning is necessary.
In STAR-CCM+ the preconditioning matrix is incorporated in the transient term, resulting in the following equation:

$$\Gamma=\begin{bmatrix}\theta & 0 & \rho_T\\ \theta_{\mathbf{v}} & \rho\mathbf{I} & \rho_T\mathbf{v}\\ \theta H-\delta & \rho_{\mathbf{v}} & \rho_T H+\rho C_p\end{bmatrix} \tag{2.41}$$

where:

- ρ_T is the derivative of density with respect to Temperature at constant pressure
- θ=$\frac{1}{U_r^2}-\frac{\rho_T}{\rho C_p}$
- U_r^2 is a reference velocity chosen in such a way that the problem results well-conditioned

Eventually, the solution of the discretized set of equations is obtained through an iterative procedure. One possibility is to use the Algebraic Multigrid Solver (AMS)-
Such procedure foresees the derivation of the equations on increasingly coarser meshes. The advantage is that an iterative procedure is convenient to reduce high-frequency errors, but performs poorly as far as low-frequency errors are concerned. For this reason, it is convenient to transfer the solution to a coarse grid, for which the remaining errors are of the high-frequency type. The procedure behind the AMS can be summarized as follows:

- combine the cells to obtain coarser mesh levels
- take the residuals from the fine level to the coarse level

- computing the residuals from the coarse level and apply them to the fine level solution

Generally speaking, the advantage of the AMS lies in that the typically the cost of a direct solution in the coarse grid is negligible with respect to a relaxation sweep performed directly on the fine grid. This approach is well suited for complex 3-D flows [7].

2.4 Parallel secant method

The parallel secant method is a root-finding algorythm, used in numerical analysis to find the root of a function. The recursive relation to be adopted is the following:

$$x_n = x_{n-1} - f(x_{n-1})\frac{x_{n-1} - x_{n-2}}{f(x_{n-1}) - f(x_{n-2})} \tag{2.42}$$

The name of the method derives from its geometrical meaning (Fig.2.5). The root of a function is found, iteratively, by finding the root of the secant between 2 points of the function itself. The method has a rate of convergence of roughly 1.62.

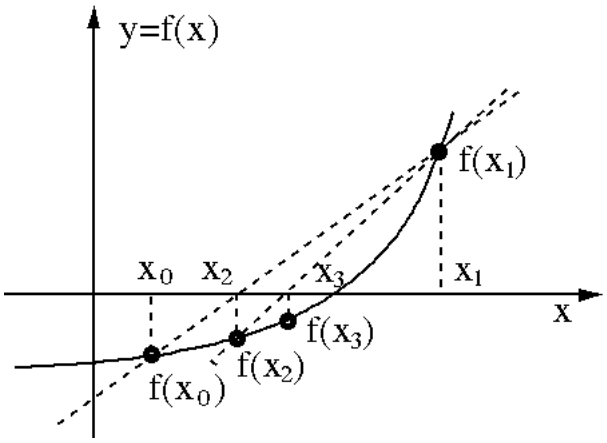

Figure 2.5: Secant method geometrical representation

2.5 Turbulated cooling pipes - experimental correlations

Plenty of effort has been in the past years to study which are the effects of turbulation on the heat and mass transfer performance of a channel.
In particular, for the case of gas turbines, the cooling channels may have different shapes, according to the level of technology and to the fluid devoted to the cooling purpose. Each case requires a separate study, due to the flow path and fluid characteristics. In this study,

circular cooling channels have been adopted.
For a circular cross section, the main geometrical parameter are shown in Fig. 2.6

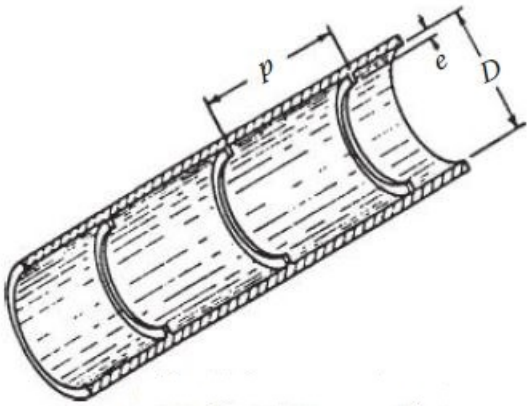

Figure 2.6: Rib-Roughened cooling channel

The geometry is described according to the following parameters:

- D = diameter
- e = rib height
- p = pitch
- $\frac{e}{D}$ = relative roughness
- $\frac{p}{e}$ = relative spacing

The correct sizing of the turbulated channels foresees a good trade-off between the inherently increased friction coefficient and the improved cooling performance of the turbulated channel with respect to the smooth one. In order to take both of them into account, the reduced pumping power and the efficiency index are introduced.
The reduced pumping power is defined as follows:

$$\frac{P_r}{P_s} = \frac{f_r}{f_s} \frac{St_s^{1/3}}{St_r^{1/3}} \tag{2.43}$$

where the subscript 'r' stands for ribbed and the subscript 's' stands for smooth. This ratio allows to evaluate the reduction in the pumping power when inlet conditions, surface area and heat load are the same. The Efficiency index, instead, is defined as:

$$\eta = \frac{St_r}{St_s} \frac{f_s}{f_r} \tag{2.44}$$

In this case, the efficiency index gives insights about the heat transfer performance of the turbulated channel with respect to the smooth one. The choice of the turbulated geometry has to be mainly driven by the maximization of both of these indices, along with manufacturing considerations.
The friction factor in a smooth channel can be computed adopting the Blasius correlation:

$$f = 0.316Re^{-0.25} \tag{2.45}$$

On the other hand, remembering that the Stanton number, can expressed as:

$$St = \frac{Nu}{RePr} \tag{2.46}$$

the Dittus-Boelter correlation has been used to compute the Nusselt number and then derive the Stanton number, namely:

$$Nu = 0.023Re^{0.8}Pr^{0.4} \tag{2.47}$$

For a turbulated channel, the correlations for the friction factor and Stanton number have been obtained by Webb et al. [8] The experiments have been carried out considering a relative spacing ranging from 10 to 40 and a relative roughness in between 0.01 and 0.02.

$$St = \frac{f/2}{1 + \sqrt{f/2}\left[4.5(e^+)^{0.28}Pr^{0.57} - 0.95(p/e)^{0.53}\right]} \tag{2.48}$$

$$\sqrt{\frac{2}{f}} = 2.5ln\left(\frac{D}{2e}\right) - 3.75 + 0.95\left(\frac{p}{e}\right)^{0.53} \tag{2.49}$$

were e^+ is:

$$e^+ = \frac{e}{D}Re\sqrt{\frac{f}{2}} \tag{2.50}$$

The correlations are valid for $e^+ > 35$ and $10 < \frac{p}{e} < 40$.
We can highlight that the friction factor is independent from the Reynolds number in this case, but it only depends on the geometry of the turbulated channels.

Chapter 3

Case Of Study

The row #1 Blade has been studied in 3 different cases which are:

- Case 1: currently adopted smooth channels
- Case 1b: smooth channels with radial temperature profile
- Case 2: turbulated channels - first configuration
- Case 3: turbulated channels - second configuration

The cases follow the introduction of new designs for the cooling network. The first case, mainly aims at evaluating the consequences of the Anima in terms of mass flow rate of coolant and the cooling performance of system. For the turbulated channels, an initial geometry has been proposed, which was later optimized, to meet the requirements of heat dissipated.
A summary of the geometrical characteristics of the channels is present in Tab. 3.1.

	Case 1	Case 2	Case 3
External diameter [mm]	Group 1: 2.44 Other groups: 1.52	Group 1: 2.44 Other groups: 1.28	Group 1: 2.44 Other groups: 1.52
Internal diameter [mm]		Group 1: 2.14 Other groups: 0.98	Group 1: 2.14 Other groups: 1.33
Rib pitch [mm]		1.6	1.6

Table 3.1: Geometrical characteristics of the channels

3.1 PH4165-Cooling Network

The PH4165 software is a Westinghouse product which performs the simulation of the cooling network of a gas turbine. It represents the starting point for the setup of the

CFD simulations of the blade, as it returns the boundary conditions for the fluid-dynamic problem.
The implementation of the cooling network in the PH4165 is the typical one of a thermal network, where all the elements are modelled resorting to the 1-D theory. The system is made up of pipes, which represent the path of the cooling air, and chambers, which set the boundaries of the pipes. The mass flow rates are defined in each pipe, wheres pressures and temperatures are defined in each chamber. The software treats the losses of the cooling network resorting to 5 different types of elements:

- R: Restrictions
- S: Seals
- V: Vortices
- F: Fractional loss
- L: Frictional loss

The elements are assembled, to build the path of the coolant throughout the machine. The software requires pressures as boundary conditions, and the definition of the Temperature in each chamber of the model. Regarding the losses, the geometrical parameters of the actual machine are provided, in order to compute the pressure drops through each pipe. The solution is obtained through an iteratiove procedure, in which all the pipes are considered adiabatic. All the elements, except the friction losses, are treated as non-ideal nozzles, for which the discharge coefficient has to be provided. The flow in a pipe is studied as a compressible adiabatic flow. At the initial phase, a reference direction for the flow in the pipes has to be assigned, then the software proceeds with the investigation of both directions to correctly predict the path of the coolant.
As said before, the fluid-dynamic of the elements is referred to the one of a nozzle. The quantity which is of interest is then the characteristic mass flow rate, defined as:

$$MFR_{char} = MFR\sqrt{\frac{T_{in}}{T_{std}}}/\frac{p_{in}}{p_{std}} \tag{3.1}$$

The definition of the geometry and of the discharge coefficient, allows to the match the characteristic mass flow rate, with the pressure ratio for each element.
To this end, 5 points of the correlating curve are needed (0%,40%,90%,95% and 100% of characteristic MFR and the corresponding pressure ratio). This points are then interpolated to obtain the characteristic curve of the equivalent nozzle, through the following correlation:

$$y_i = 10\sqrt[a]{x_i}(1+x_i)^b(1+x_i^2)^c(1+5x_i^2)^d(1+5x_i^2)^e \tag{3.2}$$

Eventually the solution is obtained through the *Paralled Secant Method.*
The main advantage of the software is that, it is an easy way to study a very complex flow path. In addition to this, it has proved to match the real fluid-dynamic conditions in the old configurations of the machine. Main limitations of the software are:

- Accuracy: As all iterative procedure, computation is stopped when a certain tolerance is reached. It may happen that convergence for a specified accuracy is not reached tough.
- Heat Transfer: The software relies on an a-priori definiton of the tempertures in each chamber, whereas all the pipes are considered adiabatic. For this reason, the actual evolution of the temperature inside the cooling network cannot be obtained and consequently the heat transfer performance of the network cannot be assessed.
- Limited modelling capability: the software can handle 5 types of loss elements, requiring the geometry as input, so that complex phenomena are reduced to a very simple modelling which may be not enough.

Taking into account all the previous considerations, the software has been used for the definition of the fluid-dynamic conditions at the inlet. As far as the thermal problem is considered, the PH4165 results are hardly reliable and the implementation of a CFD model is necessary.

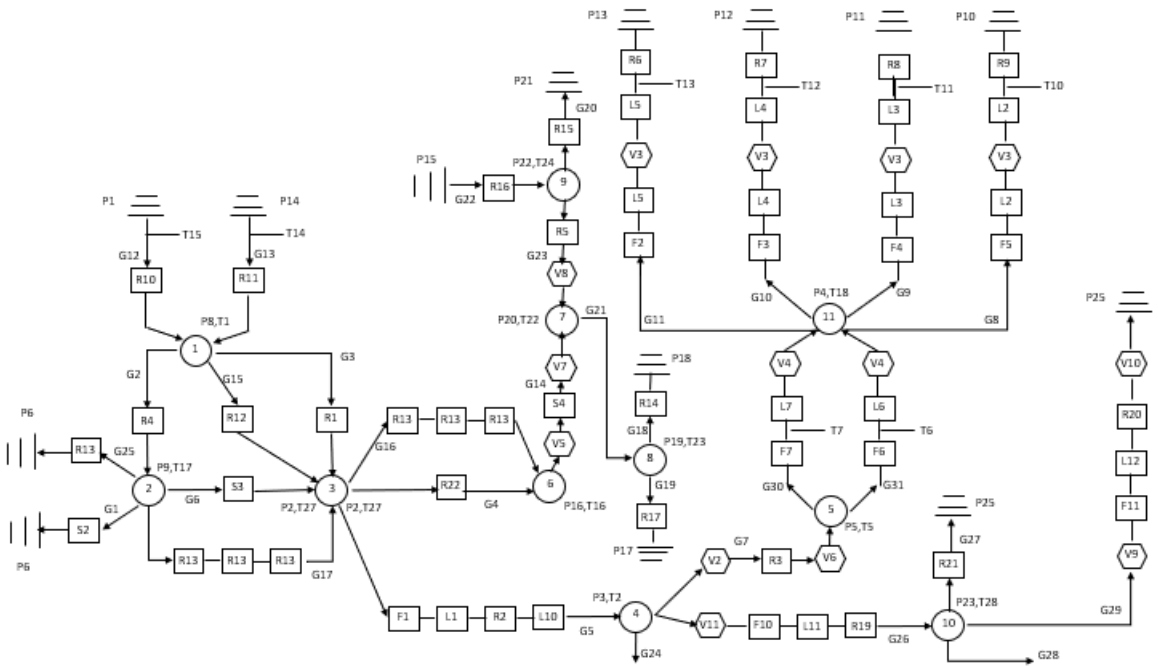

Figure 3.1: Rotor Cooling Network

3.2 Mesh generation

To complete the setup of the model, a polyhedral mesh is adopted as the most suitable to simulate complex flows. An advantage of the polyhedral mesh is that the final mesh contains about 5 times fewer cells than the tetrahedral one, starting from the same surface preparation. (Fig. 3.2). For the generation of the mesh, a surface remesher has been used to correctly capture tiny features of the geometry such as ribs and avoid any distortion of the actual geometry. The surface remesher has allowed to overcome bad triangulation coming from the CAD imported. The final mesh has been obtained with a base size equal to 1 mm and 4 prism layers to correctly simulate the flow close to the interface with the blade. In order to reduce the overall amount of cells, the density of the mesh in the solid was lowered to 80 % of the one in the fluid.
Due to the different geometries adopted, the final number of cells for the 3 cases is different. A summary of the cells counting is present in Tab. 3.2.

	Case 1	Case 2	Case 3
Solid cells	3'785'063	4,448,477	4,619,926
Fluid cells	1'883'312	2,592,805	2,813,974
Total cells	5'668'375	7,041,282	7,433,900

Table 3.2: Mesh summary

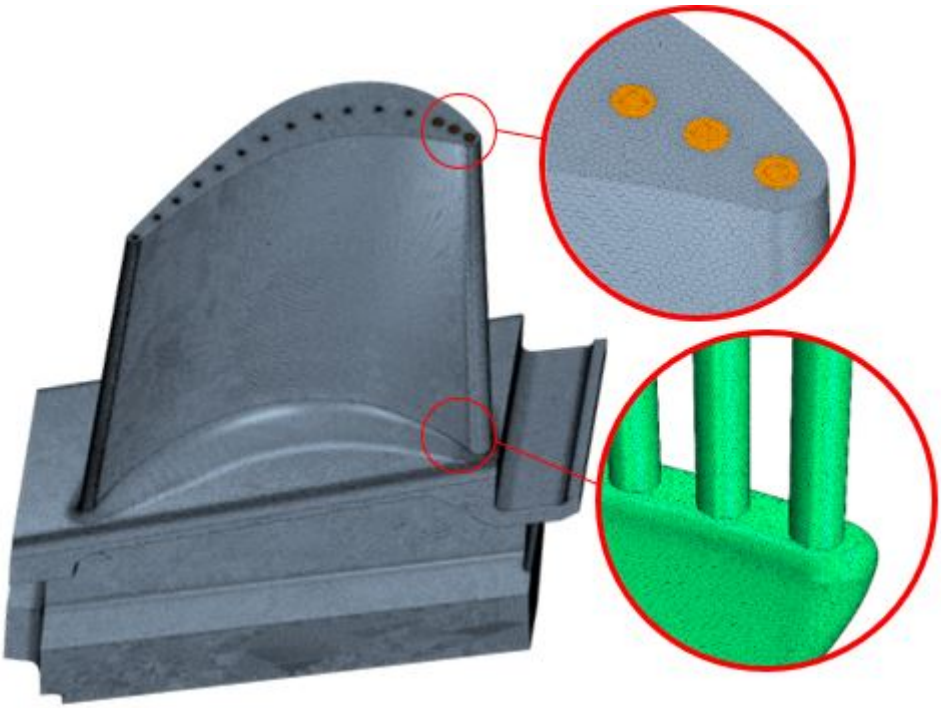

Figure 3.2: Mesh Detail

3.3 Case 1: Smooth channels

The first case of study is the characterized by smooth channels with an Anima core. This case represents the original modification of the standard blade, without accounting for the effect of rotation on the mass flow rate and heat transfer. The geometry is represented in Fig. 3.3

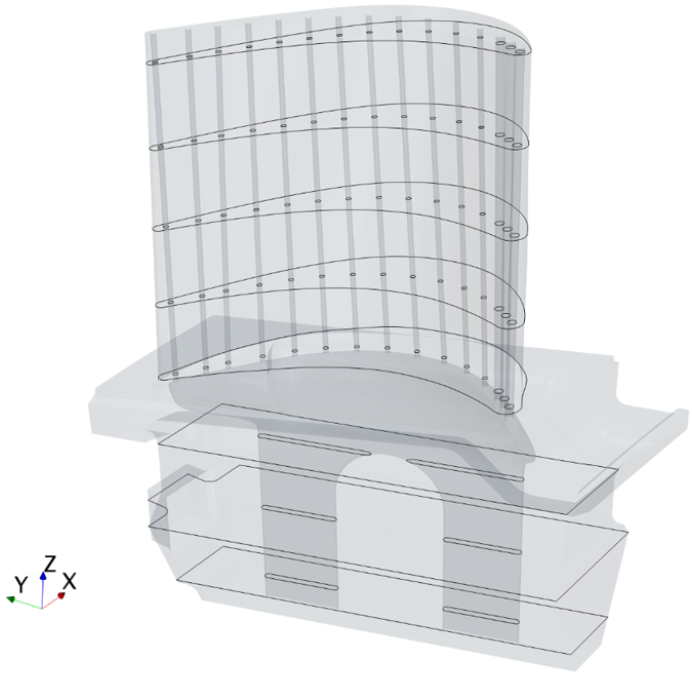

Figure 3.3: Smooth channels geometry

The boundary conditions are taken from the PH4165 software, providing both the inlet temperature and pressure for the two arms of the core. On the other hand, at the outlet of the channels, the pressure is imposed, considering a fully developed flow both for the dynamic problem and for the thermal problem. These are represented in Fig. 3.4 and 3.5. For the thermal problem, the temperature has been imposed over the blade profile and root. The Temperature field comes from a FEM simulation performed in Ansys. The main assumption here made, is that the external temperature is not highly affected by the cooling scheme adopted. This has been demonstrated, running several simulations, assuming varying heat transfer coefficients for the cooling flow. It was seen that the external temperature changes of 1^oC at maximum [9]. The main role in this case is played by the primary flow around the blade. For this reason the effect of different heat transfer coefficients and mass flow rates devoted to cooling has been neglected for the purpose of this thesis (Fig. 3.6).

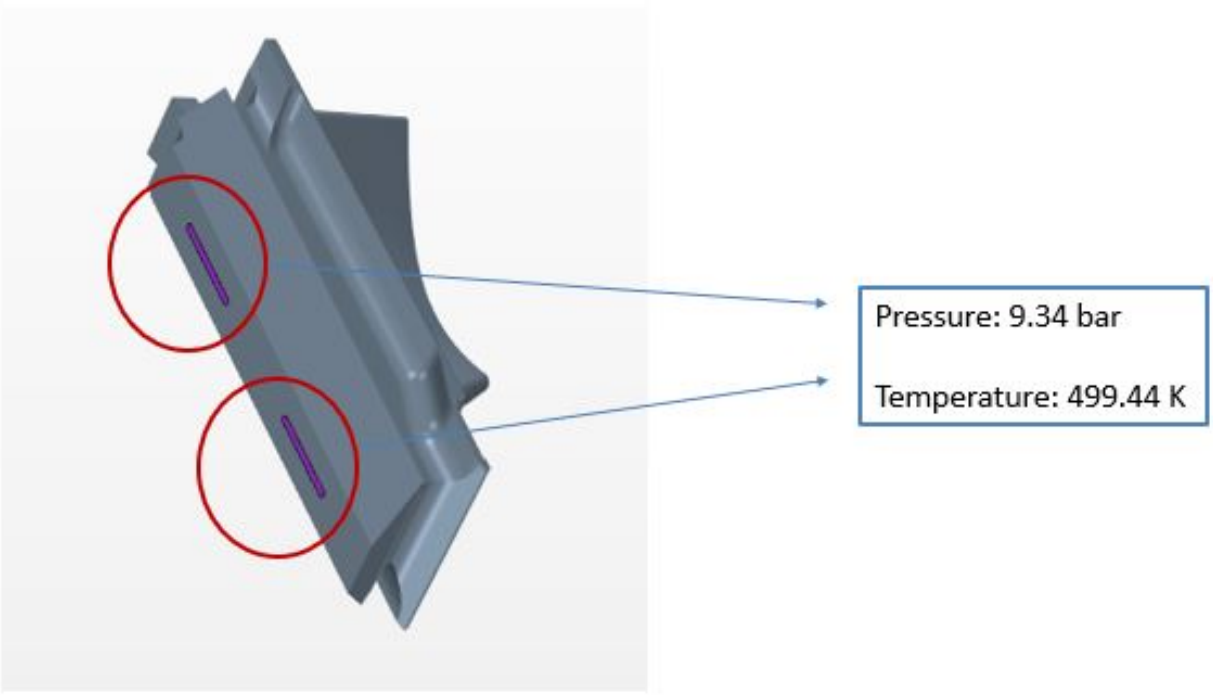

Figure 3.4: Inlet boundary conditions

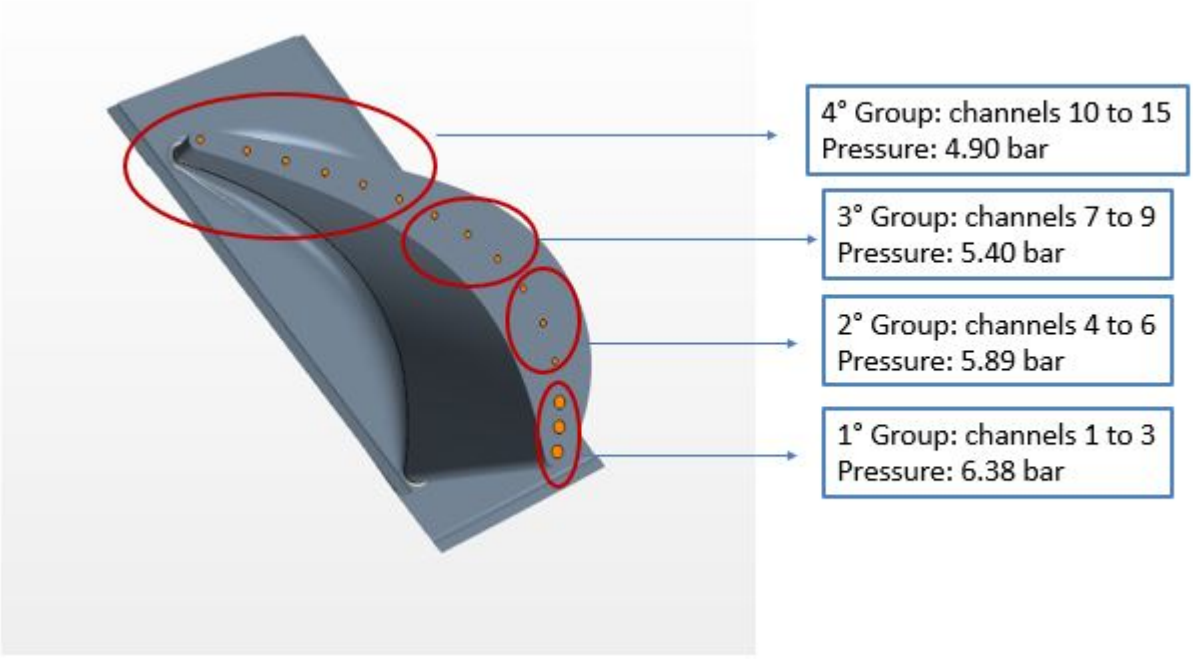

Figure 3.5: Outlet boundary conditions

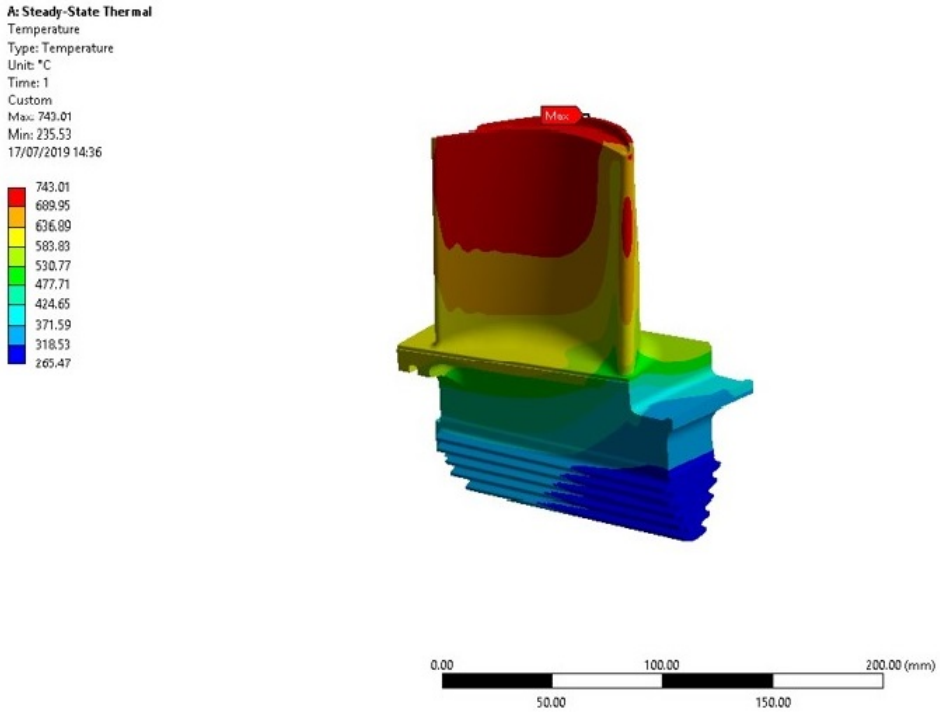

Figure 3.6: Temperature Field - Thermal Problem Boundary Condition

The analysis of the velocity Streamlines (Fig. 3.7), allows to evaluate the main consequence of the Anima region. Two stagnation zones arise in correspondence of the expansion region after the arms. Being the geometry asymmetrical, the leading edge (LE) and the trailing edge (TE) are subject to different conditions. As a matter of fact, the TE stagnation zone is not present at the LE side, since the flow directly feeds the channels of the first group. This does not occur at the TE because of the larger zone where the fluid can expand and the higher fluid-dynamic resistance of the last group's channels (which have a smaller diameter than the first group's ones). The MFR for each channel are compared with the results obtained through the PH4165 (Tab. 3.3). Indeed the latter has proved to be reliable for the simulation of straight channels, but cannot comply with complex geometries such as the Anima. The analysis of the different results highlights the aforementioned shortcomings of the old-devised software with respect to current CFD software. The most striking result is that, despite the different outlet pressures applied, the channels of the 2^{nd}, 3^{rd} and 4^{th} group deliver almost the same mass flow rate. In this case, keeping in mind the non-uniform distribution of the velocity at the inlet, the major role is played by the size of the diameters. For such small diameters, even changes of 0.5 to 1 bar in the pressure drop along the channel, may result in a slight change in the mass flow rate, as the fluid-dynamic resistance imposed is very high. It is clear that, despite the usefulness of the PH4165 software to account for the flow in the cooling network, it cannot predict the expansion of the flow before the inlet section of the cooling channels. For this reason the main differences are concentrated on the sides of the region and in the central

zone, where stagnation and mixing between the flows occur. The largest discrepancy between the estimated values is found for the channel #14 which experiences the highest pressure loss at the entrance, as can be seen by the Fig. 3.9 In addition, the results show that the CFD simulation returns a lower mass flow rate for each channel. This comes to be since the cooling network simulation does not account for any heat transfer between the solid and the fluid, and all the changes in density are accounted for through some nodal temperatures defined in the chambers of the network.

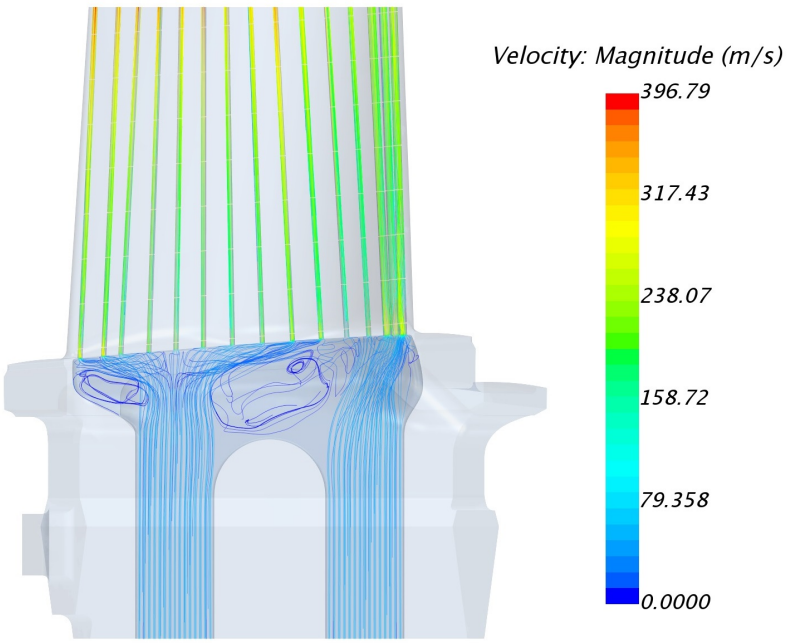

Figure 3.7: Velocity Streamlines

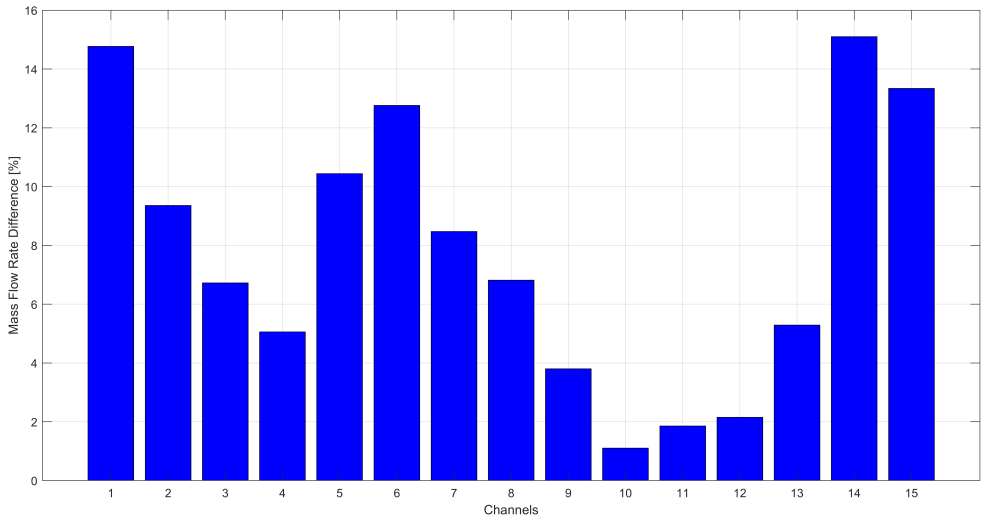

Figure 3.8: Mass Flow Rate percentage difference

Channel #	CFD MFR [g/s]	PH4165 MFR [g/s]
1	3.89	4.63
2	4.19	4.63
3	4.32	4.63
4	1.54	1.62
5	1.46	1.62
6	1.42	1.62
7	1.51	1.64
8	1.53	1.64
9	1.58	1.64
10	1.62	1.64
11	1.61	1.64
12	1.61	1.64
13	1.56	1.64
14	1.40	1.64
15	1.42	1.64

Table 3.3: Mass Flow Rates Comparison CFD-PH4165

Figure 3.9: Inlet Sections - Channels #13 to #15

Beside the effect of the stagnation region on the distribution of the velocity at the inlet of the channels, the stagnation zone is very harmful for the heat transfer performance of the

cooling system. As a matter of fact, the low velocity limits the heat transfer coefficient of the anima, resulting into a higher temperature of the solid at the interface. Despite the peak in temperatures, the root can withstand temperatures of the order of 600-700^oC, and this is not to be considered a major issue for the resistance of the blade.
The contribution of each channel to the cooling purpose is shown in Fig. 3.11. At the leading edge, more heat is dissipated thanks to the larger diameter. This, in turn, determines a larger mass flow rate and surface devoted to heat transfer. On the other hand, the intermediate channels undergo a reduced heat exchange, mainly due to the lower amount of air flowing through them. Regarding the last channels, the trend follows the distribution of mass flow rate into the channels, and a little difference is addressed to the non uniform distribution of temperature over the profile and to the changing thickness of the solid at the TE.

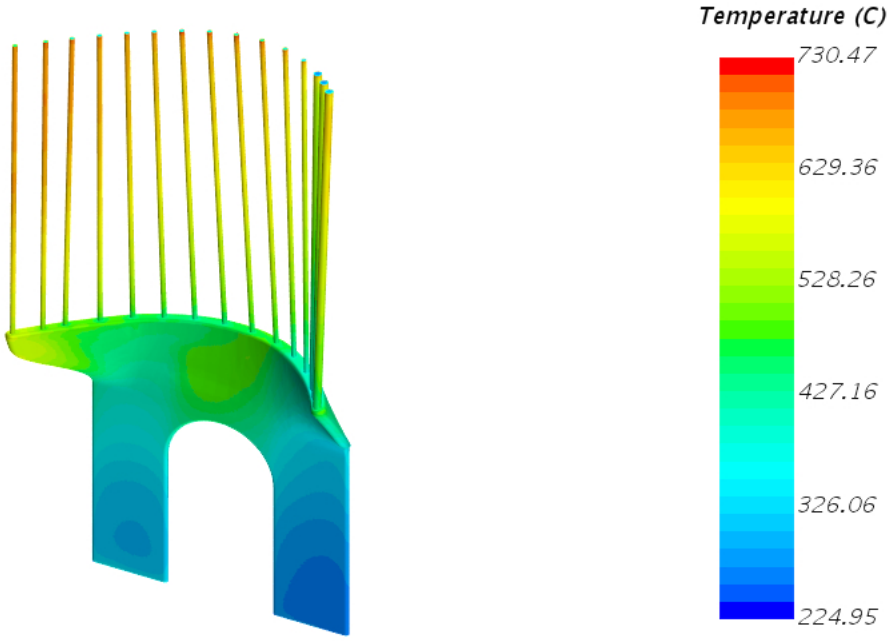

Figure 3.10: Temperature at the Solid-Fluid interface

The main analysis of the current geometry is the the evaluation of the heat transfer coefficients featuring the channels. The computation has been performed for 4 different channels, 1 for each group (Fig. 3.12, 3.13, 3.14, 3.15). Figures show how the heat transfer coefficient of each channel tends to be higher at the inlet, and tends to stabilize as it develops through the length. The reson behind this is that the flow pattern at the entrance region permits a higher heat transfer with respect to the fully developed zone, where the flow is organized. At the entrance, instead, a disordered flow patterns allows a better mixing between the core flow and the one close to the wall, thus dissipating the

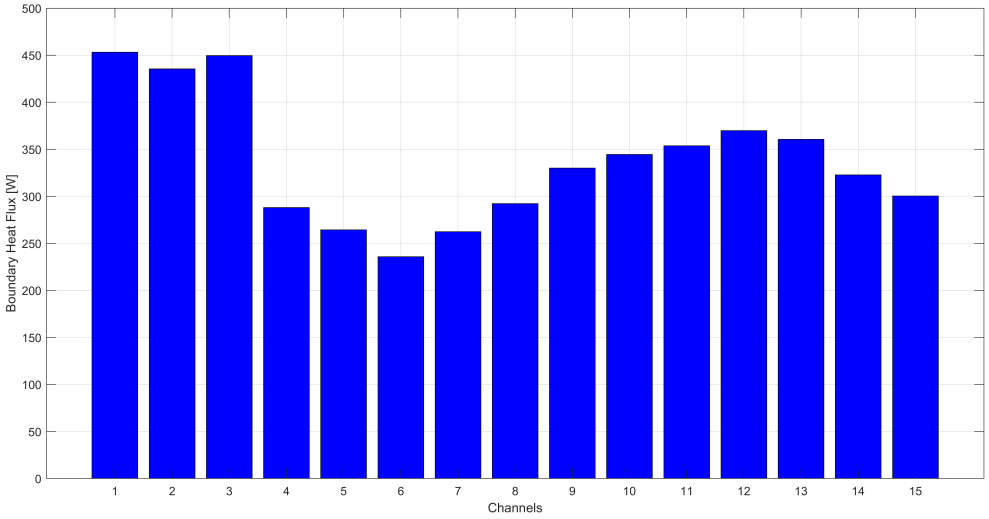

Figure 3.11: Boundary heat flux through each channel

heat in a more efficient way. Tab. 3.4 shows the agreement of the heat transfer coefficients obtained through the CFD simulation, with the Dittus-Boelter formulation for turbulent flows in a channel.

Channel #	Average Nusselt number - CFD	Average Nusselt number - Dittus-Boelter	Discrepancy
2	138.7	145.8	4.9 %
5	89.6	91.8	2.4 %
8	89.0	95.3	6.6 %
12	90.0	98.9	9.1 %

Table 3.4: Validation of the results

As far as the channel 5 is concerned, the high heat transfer coefficient by the end of the channel is addressed to the imposed boundary conditions. The Temperature profile imposed over the blade surface features a peak in temperature by the outlet section of the channel #5 which leads to an increase in the heat flux and, in turn, of the heat transfer coefficient. Other than the temperature, even the position of the channel is affecting the heat transfer coefficient. As a matter of fact, this large increase in the heat transfer coefficient features the channels of the second group only, meaning that the non-uniform temperature and thickness of the blade are playing their role as well.
To verify this statement, a new simulation has been run imposing a different Temperature profile.

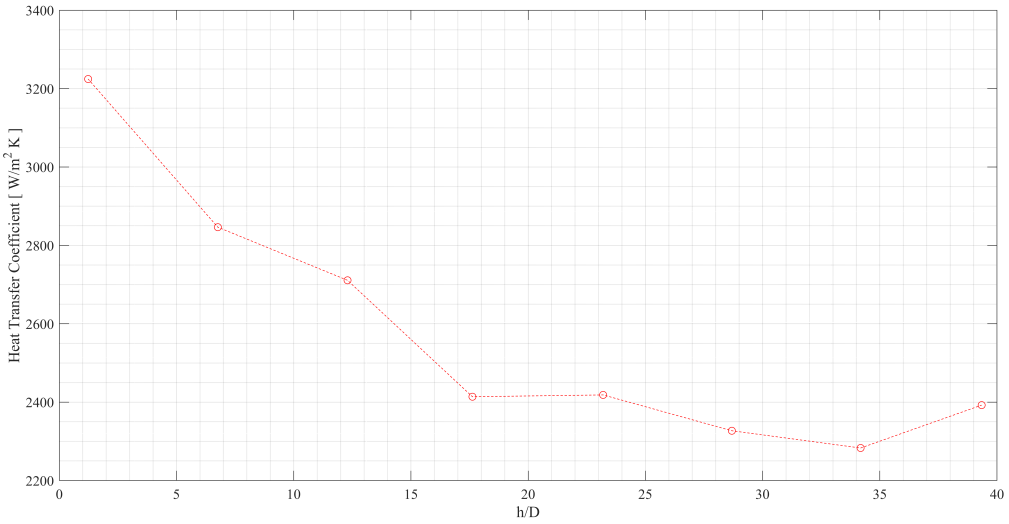

Figure 3.12: Heat Transfer Coefficient Channel 2

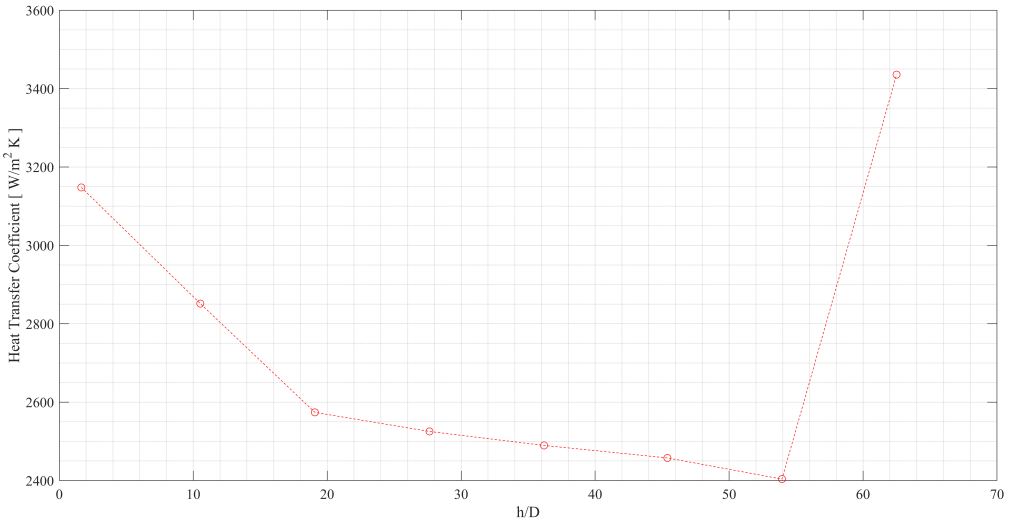

Figure 3.13: Heat Transfer Coefficient Channel 5

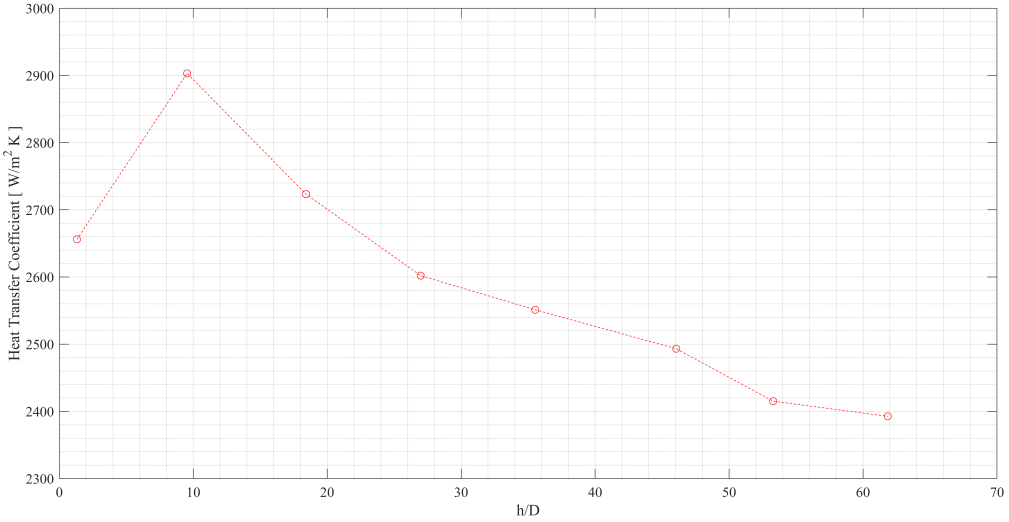

Figure 3.14: Heat Transfer Coefficient Channel 8

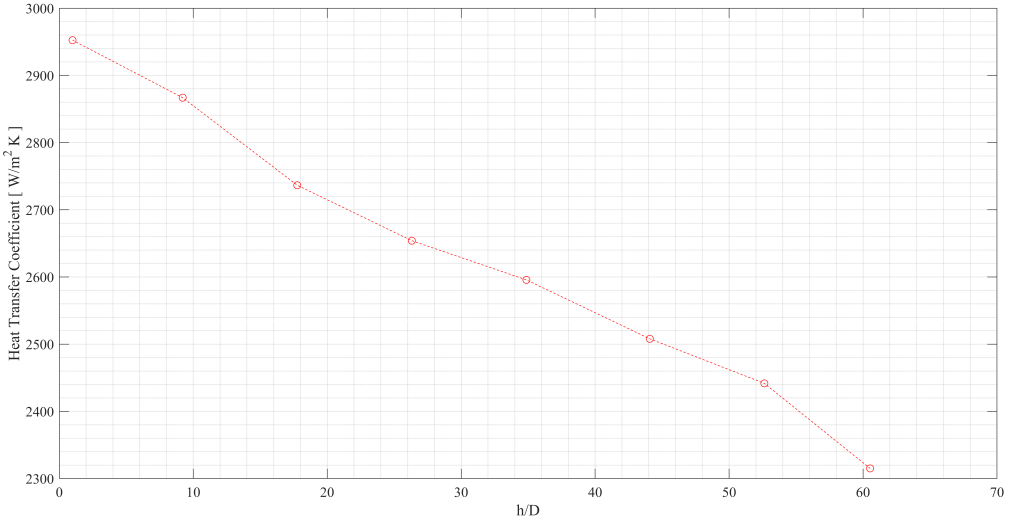

Figure 3.15: Heat Transfer Coefficient Channel 12

3.4 Radial Temperature Profile

Conserving the maximum and minimum values obtained from the FEM simulation in ANSYS, the new profile features a radially changing temperature, uniform from the LE to the TE and from the Pressure Side and Suction Side (Fig. 3.16).

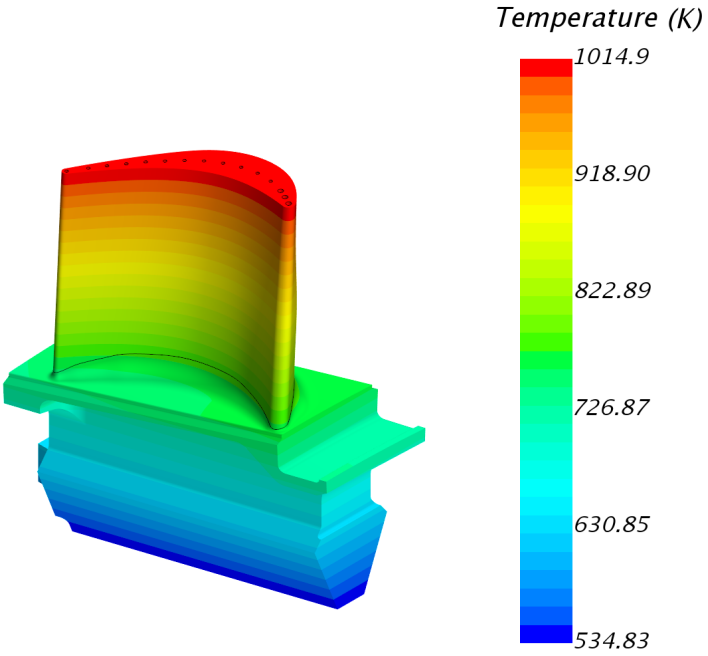

Figure 3.16: Radial Temperature profile

The analysis of the heat transfer coefficients trends, shows that for a different temperature profile, once again the peak in the heat transfer coefficient exists. It is much more marked for the channel number 5, compared to the channel number 8. We can conclude that both the temperature profile imposed and the geometry are playing an important role, affecting the heat transfer coefficient to a very high extent. It is clear that a uniformly varying temperature profile leaves time to the flow to adjust to the the temperature change, thus not leading to a very high peak in the heat transfer coefficient. On the other hand, when the temperature distribution is not uniform and presents hot spots, the suddenly increasing boundary heat flux from the solid to the coolant, paves the way to high peaks in the heat transfer coefficient.

Tables 3.5 and 3.6 evidence the differences between the two Temperature profiles which have been proposed.

The distribution in terms of mass flow rate is similar. The analysis show that in the regions which are heated more in the radial profile, the mass flow rate tends to be lower than the one predicted through the actual temperature profile. As a matter of fact, the reduction in the density of the air, determines a lower mass flow rate through the channel,

since the velocity distribution is not much affected. On the other hand, the channels which suffer from a lower boundary heat flux undergo an increase of mass flow rate exhausted. The channels of the first group undergo an increased heat flux, due to the higher temperatures reached in that zone by profile imposed over the blade. As a matter of fact, Fig. 3.6 shows that high temperatures are reached from the middle of the camber line to the TE. At the LE, instead, the temperature imposed is much lower. The largest percentage difference between the 2 cases characterizes the channels of the third and fourth group. The boundary heat flux dicreases up to 10%, compared to the actual profile, since the high temperature was reached faster than the Radial profile.

Channel #	Mass Flow Rate [g/s] Actual Profile	Mass Flow Rate [g/s] Radial Profile	Difference [%]
1	3.98	3.94	0.948
2	4.19	4.19	-0.0780
3	4.32	4.33	-0.181
4	1.54	1.56	-1.09
5	1.46	1.50	-2.75
6	1.42	1.48	-4.24
7	1.51	1.58	-4.87
8	1.54	1.59	-3.58
9	1.58	1.63	-2.94
10	1.62	1.67	-2.93
11	1.61	1.66	-3.09
12	1.61	1.66	-3.38
13	1.56	1.61	-3.44
14	1.39	1.45	-3.89
15	1.43	1.49	-4.55

Table 3.5: Mass Flow Rate comparison between the two Temperature profiles

Channel #	Boundary Heat Flux [W] Actual Profile	Boundary Heat Flux [W] Radial Profile	Difference [%]
1	434	447	-2.91
2	420	435	-3.43
3	434	439	-1.05
4	277	267	3.65
5	253	243	3.87
6	224	220	1.97
7	250	236	5.68
8	279	255	8.7
9	316	282	10.8
10	330	295	10.6
11	338	303	10.4
12	353	315	10.7
13	342	311	9.12
14	303	285	6.18
15	281	282	0.223

Table 3.6: Boundary Heat Flux comparison between the two Temperature profiles

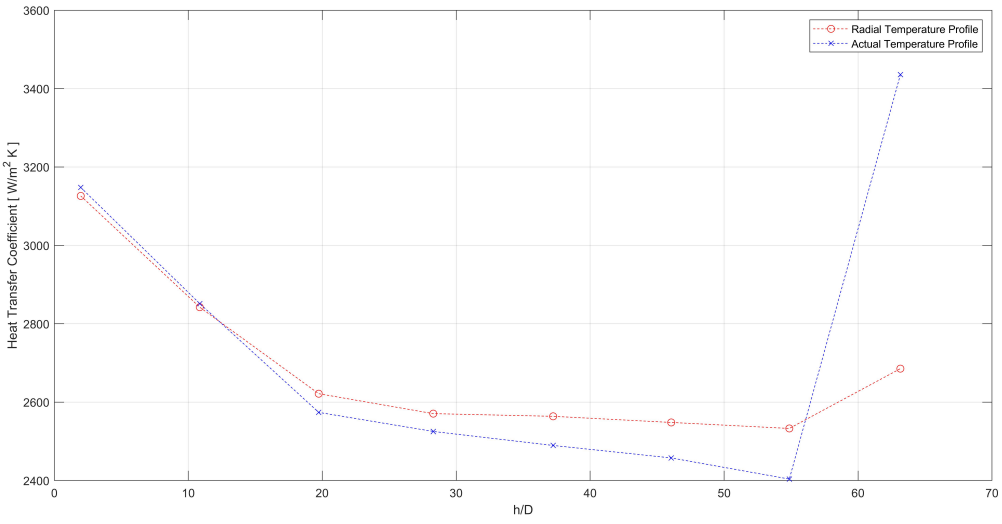

Figure 3.17: Channel 5 - Heat Transfer Coefficient

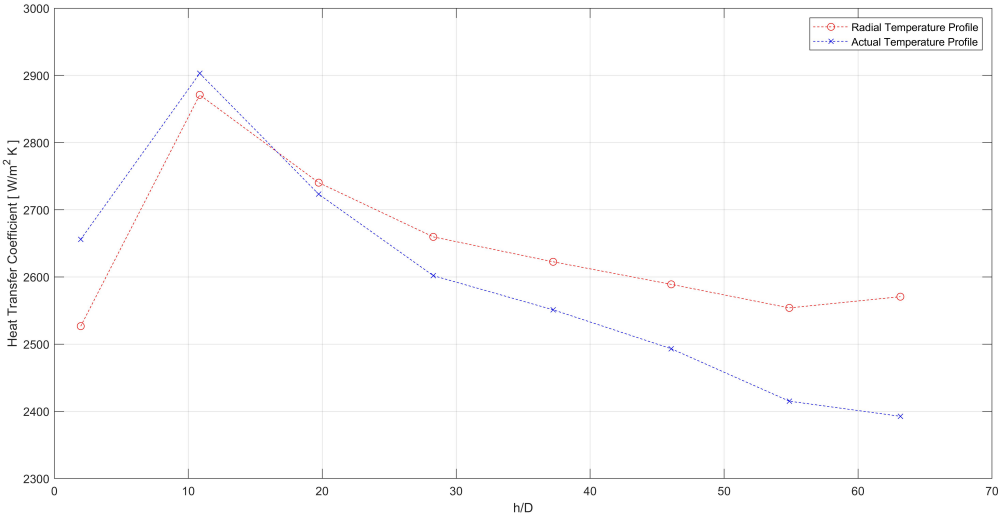

Figure 3.18: Channel 8 - Heat Transfer Coefficient

3.5 Case 2: Turbulated channels - First Geometry

The main aim of the engineers of EthosEnergy was to reduce the coolant mass flow rate, keeping the thermal response of the cooling channels untouched. To this purpose, the channels of the first group were rib-turbulated, whereas the remaining channels underwent a double modification. The external diameter was reduced, to increase the fluid-dynamic resistance and the channels have been turbulated as well.
As fas as the geometrical parameters of the rib-turbulated channels are concerned, the pitch-to-rib-height ratio and the rib relative roughness, have been chosen to resemble the channels of a machine currently produced.

3.5.1 Mesh sensitivity analysis

The greatest effort regarding a CFD simulation is spent on finding the mesh which balances the computational effort and the accuracy of the results. To this end a mesh sensitivity analysis was conducted for both the smooth and the turbulated case.
The results of the smooth channels mesh sensitivity are already presented in a previous work, [10] whereas in this work the results concerning the turbulated channels are disclosed.
In order to reduce the computational time, the mesh sensitivity was performed on a reduced model characterized by a single channel of the first group of the blade, surrounded by a portion of solid. The simulated channel has the same geometrical features as the ones of the first group.
The boundary conditions which were imposed, were taken from the PH4165 software and

are sketched in the Fig. 3.19.

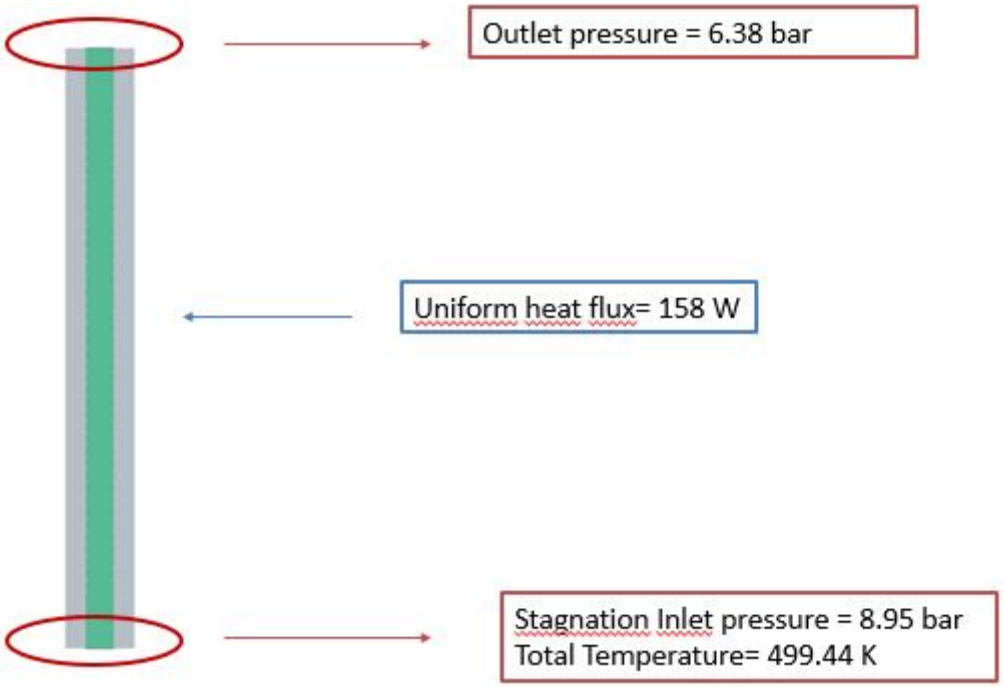

Figure 3.19: Single Channel - Boundary conditions

The analysis was mainly focused on finding the correct base size. As far as the number of prism layer is concerned, the previous analysis for smooth channels has been taken as a reference since the threshold in terms of computational resources had already been reached.
Three different base sizes were investigated:

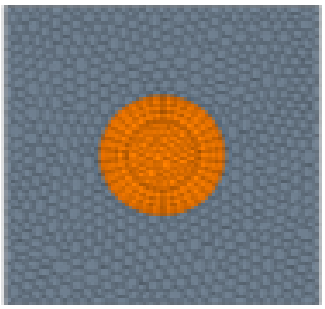

Base Size: 0.5 mm

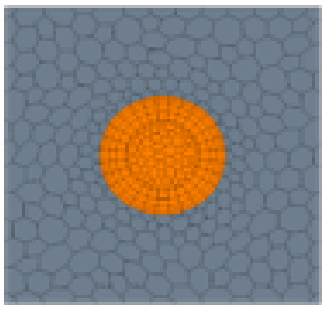

Base Size: 1 mm

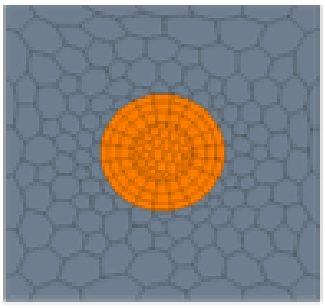

Base Size: 2 mm

The assessment of the mesh dependency was driven by the results in terms of mass flow rate and bulk temperature. Indeed a convergent MFR gives insights in terms of the dynamic performance of the channel, whereas the bulk Temperature is characteritstic of the heat transfer coefficient. When both values converge, the mesh is not affecting the results of the thermal-dynamic problem.

The Richardson's extrapolation was adopted in order to estimate the solution for an infinitely fine mesh. The necessary condition to be satisfied, to resort to the extrapolation, is that the percentage error must dicrease as the mesh is refined. The Fig. 3.20 shows the trend of the relative error for the various investigated meshes.

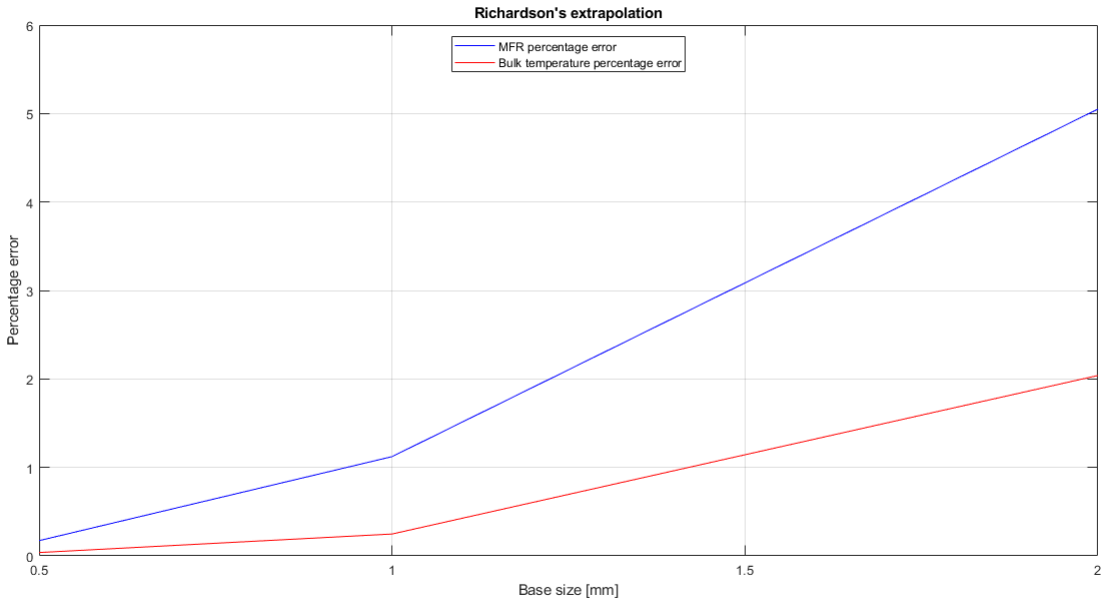

Figure 3.20: Relative Error Trend

The extrapolated values, according to Richardson's extrapolation are the following:

$$\text{MFR} = 2.10 \text{ [g/s]}$$
$$\text{Bulk Temperature} = 621 \text{ [K]}$$

Comparing the results of the simulations and the extrapolated values, a base size equal to 1 mm has been chosen thanks to the good trade-off computational effort and accuracy. In particular, the selected mesh returns an estimated error of 0.25% for the Bulk Temperature and 1.1% for the MFR. The results are summarized in the Tab 3.7.

Base Size [mm]	Bulk Temperature [K]	MFR [g/s]	Error MFR [%]	Error Bulk T [%]
2	633.7	2	5.1	2
1	619.5	2.13	1.1	0.25
0.5	620.8	2.11	0.17	$3.8*10^{-2}$

Table 3.7: Mesh Sensitivity Summary

Beyond the Richardson's extrapolation, the numerical accuracy of the results has been evaluated through the study of the Grid Convergence Index. The quantity has been

	Bulk T [%]	Mass Flow Rate [%]
CGI_{12}	0.0264	0.215
CGI_{23}	0.2881	1.40

Table 3.8: Convergence grid index values

computed both for the fine grid and for the medium one, in order to justify the choice of the medium size adopted. The results are present in Tab. 3.8. According to the Grid Convergence analysis, the medium size has been chosen and the results can be evaluated with the associated error band:

$$MFR = 2.13 \pm 1.40\% \ [g/s]$$
$$T_{bulk} = 619 \pm 0.288\% \ [K]$$

Eventually it has been checked that the results are in the asymptotic convergence range:

$$Convegrence\ Factor_{MFR} = 0.990$$
$$Convergence\ Factor_{T_b} = 1.00$$

The convergence factors are almost equal to the unity, then the solution is in the asymptotic range, meaning that any refinement of the grid would lead the results to approach the numerical asymptotical solution. Fig. 3.21 shows the velocity distribution of the flow over the rib. The main characteristics are the recirculation zones right before and after the rib and the detachment of the flow over the rib tip.
These affect the distribution of the heat transfer coefficient, which is enhanced where recirculation happens, because the hot fluid close to the wall is easily mixed with the colder bulk flow.

3.5.2 Validation of the results for a single channel

The single channels results were tested against the correlations discussed in section 2.5. The geometrical parameters of the channel are the following:

$$\frac{p}{e} = 10.67$$

$$\frac{e}{D} = 0.061$$

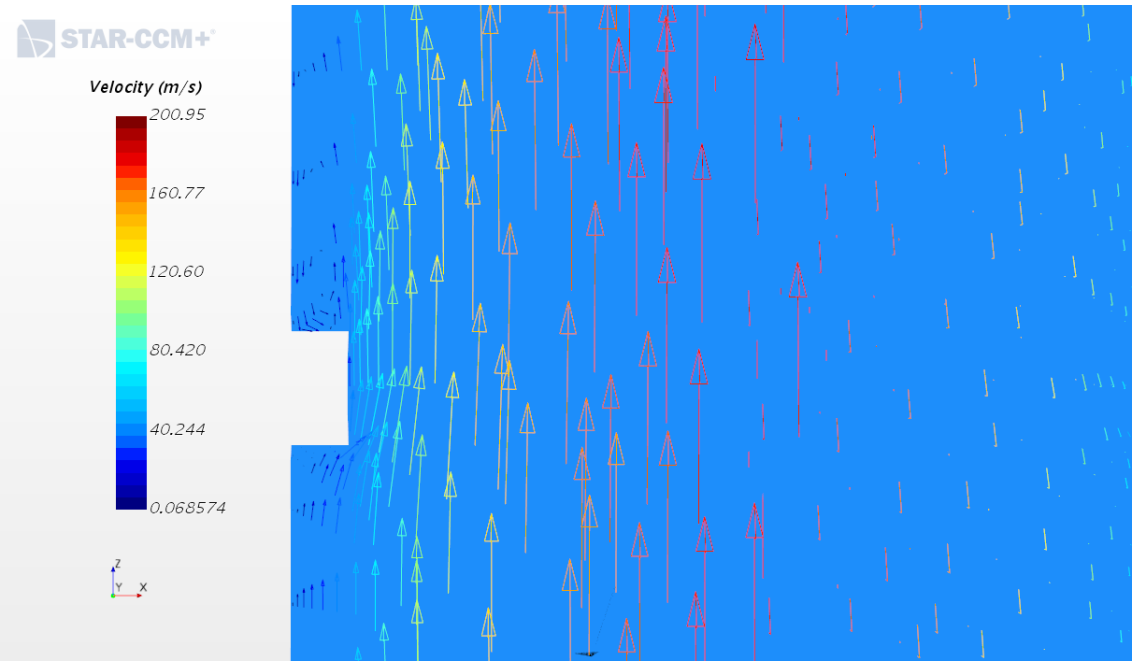

Figure 3.21: Velocity distribution by the ribs

The resulting Stanton number, according to the correlations is:

$$St = 0.0096$$

The computation of the average Stanton number from the CFD simulation has been carried out in the following manner:

$$h_{av} = \frac{q''}{(T_w - T_b)_{av}}$$

$$\frac{1}{(T_w - T_b)_{av}} = \frac{\int_0^L \frac{dx}{(T_w - T_b)_x}}{L}$$

$$Nu_{av} = \frac{h_{av} * D}{k}$$

$$Re = \frac{4 * MFR}{\pi \mu D}$$

$$St = \frac{Nu}{RePr}$$

The resulting Stanton number from the CFD simulations is 0.0095.
Despite the good agreement between experimental correlations and a parameter which is inherently affected by both the fluid-dynamic and the thermal response of the channel (we can remember that the Stanton number is equal to the ratio between the heat transfer

coefficient and the thermal capacity), the validation of the results cannot be considered satisfying. On one hand, the model adopted and the mesh used, have not been tested against a point-like analysis, to assess the prediction of the flow distribution over and after the ribs. As a matter of fact, the flow pattern is what determines locally the heat transfer coefficient, and in a global sense affects the pressure drops along the channel. On the other hand, the lack of experimental results for this kind of geometry makes it almost impossible to go further with the validation of the results.

3.6 Case setup - Rib-roughened cooling channels

When turbulated cooling channels are simulated, a modification of the boundary conditions is necessary. As a matter of fact, the increase in the friction factor in turbulated cooling channels, has the major effect of reducing the MFR devoted to the cooling purpose, on one hand, and increasing the pressure lossed on the other. For this reason, the pressure at the inlet of the cooling channels is expected to increase, thus mitigating the enhanced friction losses.
Once again, in order to resort to the correct boundary conditions, the software PH4165 was used to evaluate the whole cooling network, and update the pressure boundary conditions [11] .
The software has been overwritten in order to treat the channels as turbulated cooling channels instead of smooth channels. The relationship for the heat transfer coefficient was taken from the correlation proposed by Webb, introduced in section 2.5. On the other hand, instead, it was seen that the Surface Temperature of the blade is affected by the heat transfer coefficient of the cooling channels, to a very low extent, and mainly depends on the TIT [9]. For this reason the BC for the thermal problem remained unchanged in all the different configurations. As far as the boundary conditions for the fluid-dynamic problem are considered, the inlet pressure is raised, leaving the outlet pressure untouched. A summary of the boundary conditions applied to the system is reported in Fig. 3.22, 3.23, 3.24 .

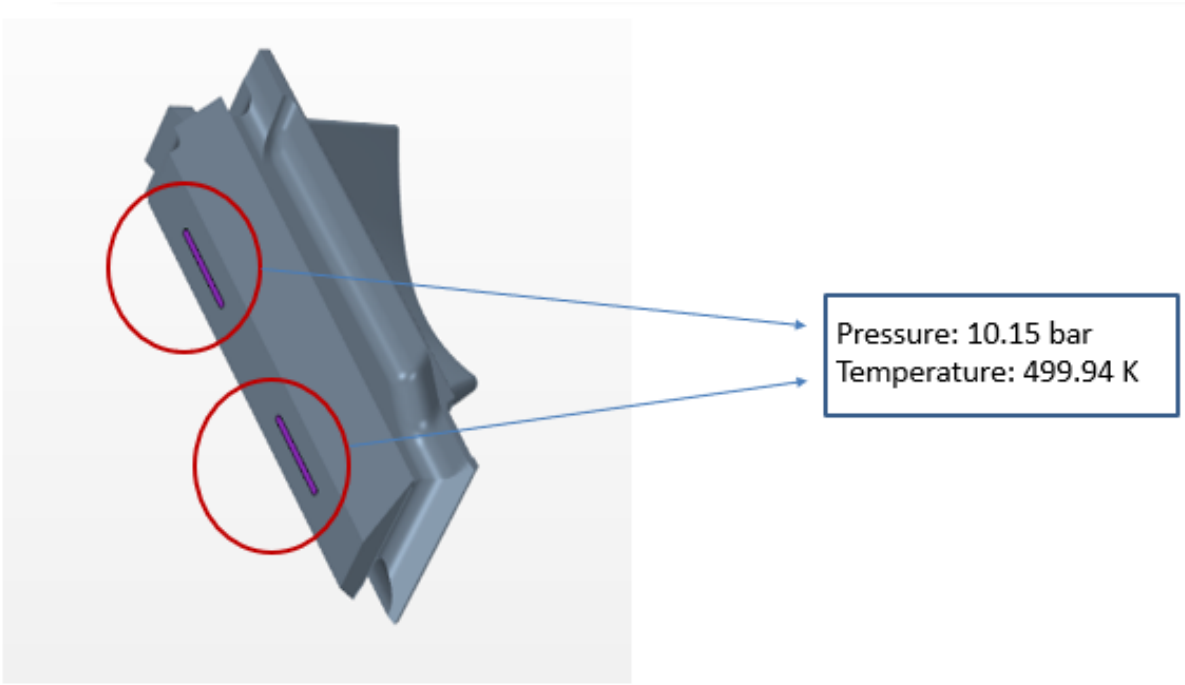

Figure 3.22: Inlet Boundary Conditions - Turbulated channels

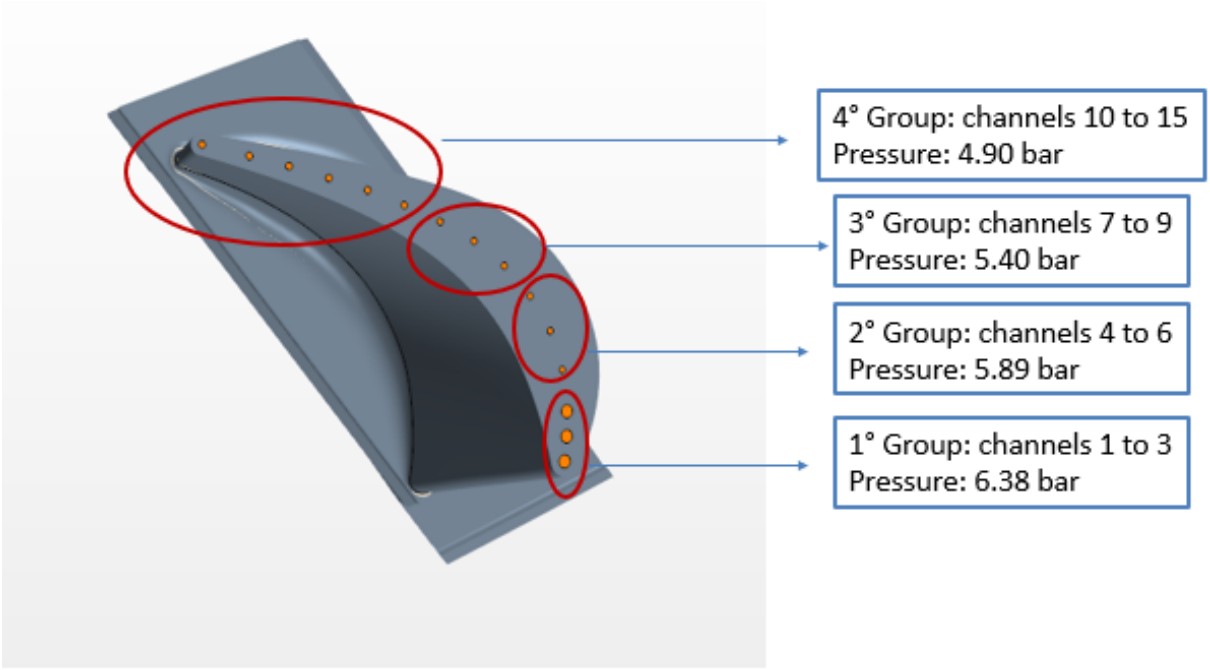

Figure 3.23: Outlet boundary conditions - Turbulated channels

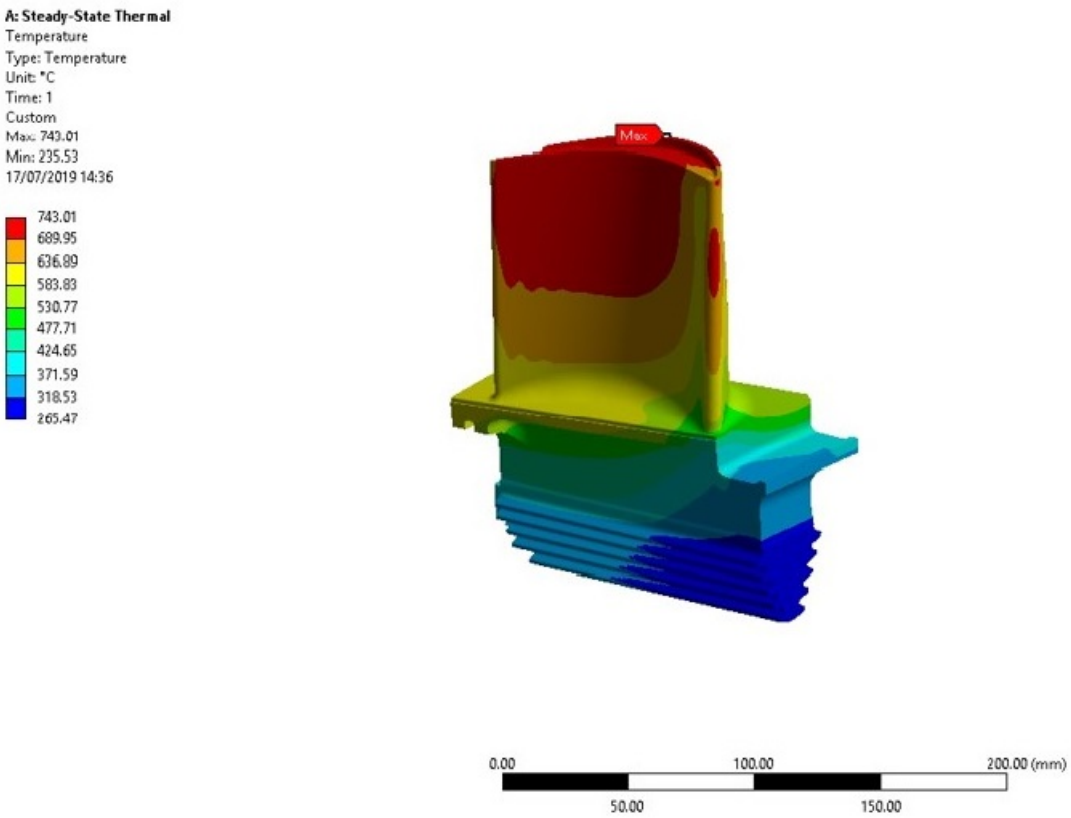

Figure 3.24: Temperature profile - Turbulated channels

The first comparison between the turbulated geometry and the smooth case concerns the mass flow rate of air devoted to the cooling purpose (Fig. 3.25). The total mass flow

rate is reduced from 31.08 g/s to 10.28 g/s, resulting into a third of the design case. The main effect can be seen both in the modification of the stagnation zones and the different temperatures reached in the internal part of the blade for the same external one (Fig. 3.26, 3.27). As shown in the figure, the stagnation zones are much reduced as a consequence of the lower velocity at which the mass flow rate fills the Anima and later the channels. As said before, the stagnation zones were detrimental for the heat transfer between fluid and solid, thus leading to a temperature peak. In this case the negative effect is mitigated and the temperature profile at the interface between solid and fluid is more homogeneous. The same happens for the secondary stagnation zone, which caused a heterogeneous feeding of the channels of the last group. In this case the mass flow rate distribution over the channels is regular and mainly determined by the change in the sections from the 1^{st} group to the others.

The first thing to notice is that, despite the different outlet pressures, the channels of the 2^{nd} to the 4^{th} group deliver almost the same mass flow rate. Indeed, since the diameter of the channels is very small, the fluid-dynamic resistance opposed to the passage of the flow is very high. The outcome is that the mass flow rate is almost unchanged among the last 3 groups, despite the different outlet pressures.

Even though the distribution of the flow is more homogeneous, still side-effects exists. The mass flow rate feeding channel # 1 is slightly lower than the one feeding channels # 2 and 3 due to the expansion in the Anima core.

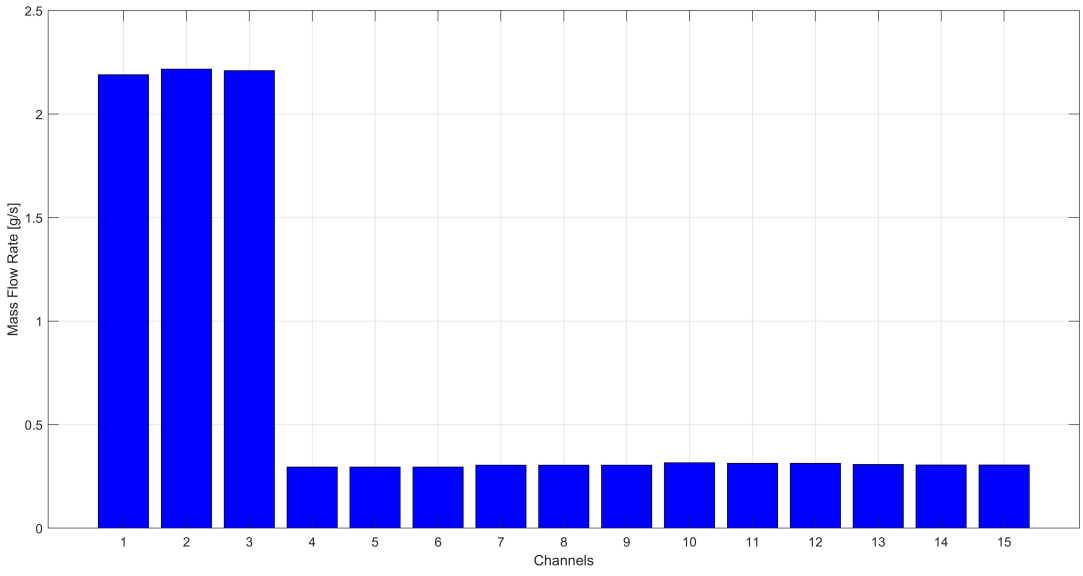

Figure 3.25: Mass flow rates - Turbulated channels

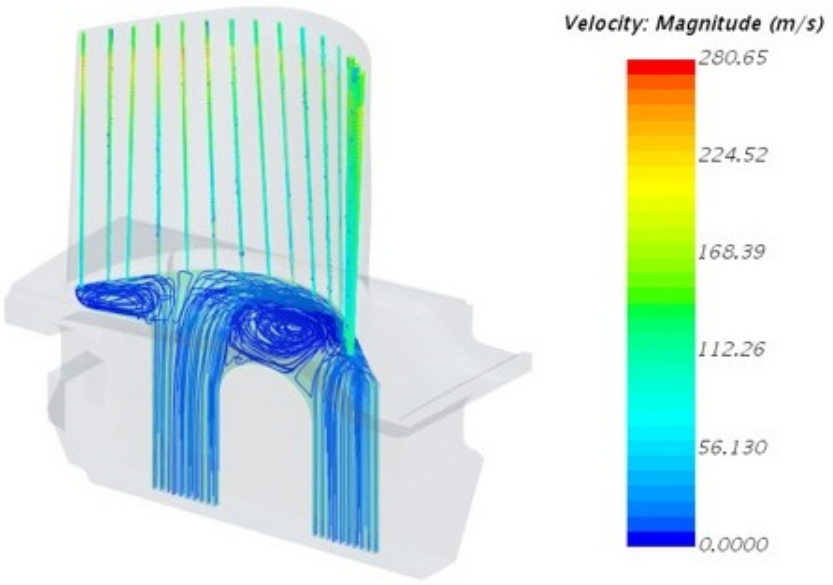

Figure 3.26: Velocity streamlines - turbulated

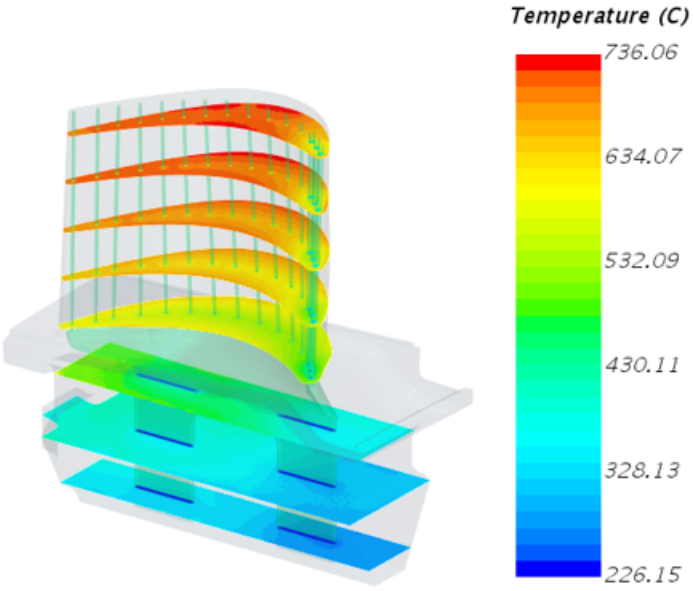

Figure 3.27: Temperature development across various sections

By comparing the results coming from the smooth and turbulated case, both the drawbacks and the benefits of these turbulators can be appreciated. To highlight this a performance index is introduced which is the same as the one in equation... but applied to global quantities. The performance index is computed as:

$$PerformanceIndex = \frac{Q_{turbulated}}{Q_{smooth}} \frac{MFR_{smooth}}{MFR_{turbulated}} \tag{3.3}$$

The highest effect is experienced by the central channels, compared to the external ones.

On the other hand, the total boudary heat flux is reduced to a too high extent and it is not sufficient to cool down the blade properly. It passes from the 6390 W to 3250 W which is not enough.

Channel #	Smooth MFR [g/s]	Turbulated MFR [g/s]	Smooth Heat Flux [W]	Turbulated Heat Flux [W]	Performance index
1	3.89	2.19	434	374	1.53
2	4.19	2.21	420	340	1.53
3	4.32	2.21	434	337	1.52
4	1.54	0.295	277	85.7	1.62
5	1.46	0.295	253	100	1.96
6	1.42	0.295	224	109	2.34
7	1.51	0.305	250	118	2.34
8	1.53	0.305	279	120	2.16
9	1.58	0.305	316	121	1.98
10	1.62	0.316	330	125	1.94
11	1.61	0.314	338	122	1.85
12	1.61	0.314	352	125	1.82
13	1.56	0.308	342	112	1.66
14	1.40	0.304	304	106	1.6
15	1.42	0.305	281	92.1	1.53

Table 3.9: Comparison smooth - turbulated channels

The heat transfer coefficients have been evaluated in 38 sections for each channel. 36 of these sections lie in the rib-turbulated portion of the channel, and are alternatively placed over a smooth portion and a rib-turbulator. The first 2 sections, instead capture the heat transfer at the entrance of the channel.
Once again, the central channel of each group has been selected as the characteristic one for the group itself. Fig. show the heat transfer coefficient trend along the channel
We can see that in correspondence of the ribs, the heat transfer coefficient increases even by 45% with respect to the correspoding smooth part. Another interesting feature common to all the channels, is the reduction in the heat transfer coefficient which is present in the entrance region. The last part of this section is dedicated to the analysis of the Nusselt number of the channels. The main aim is to investigate where modifications are necessary, in order to leave the total heat exchanged untouched.

Channel #	Average Nusselt Number Smooth Channels	Average Nusselt Number Turbulated Channels	Average Nusselt Number Smooth Channels - Same Reynolds
2	138.7	143.2	87.2
5	89.6	71.72	29.29
8	89.0	72.96	30.09
12	90	71.93	30.79

Table 3.10: Nusselt Number Comparison

As we can see from the table, the Average Nusselt number increases for the channel 2, whereas it is less than the corresponding Nusselt number of the initial smooth channels. The main drawback of this proposed geometry is that the reduction of the diameter of the channels of the last groups which is affecting the total mass flow rate devoted to cooling to a too high extent, thus inhibiting the channels to exchange enough heat to keep the blade cold.
The Tab. 3.10 highlights the results for 3 different cases.
The second column refers to the average Nusselt number of the smooth channels (Case 1), the third column refers to the average Nusselt number of the first turbulated geometry (Case 2) and the fourth column referers to the average Nusselt number of a smooth channel characterized by the same Reynolds number and external diameter as the turbulated one. We can see that in all the cases, the value for turbulated channels is higher than the one for the corresponding smooth channel (fourth column). The low value of the Nusselt numbers in the last column are due to the very low mass flow rate through the channels 5,8 and 12. Indeed, such low mass flow rates lead to a transitional turbulent flow. More than this, the interesting outcome is that for the small channels, the smooth configuration is more convenient with respect to turbulated one. This is caused by the huge reduction of mass flow rate from the smooth geometry to the turbulated one (Tab. 3.9). As a matter of fact, a lower mass flow rate determines a lower Reynolds number which characterizes the flow distribution inside the channels. The lower is the Reynolds number, the more organized is the motion, then the lower is the heat transfer coefficient.
This is detrimental, beacuse not only less mass flow rate is devoted to cooling, but also the heat flux has been penalized by the reduction in the heat transfer coefficient.
From these considerations, a new turbulated geometry has been proposed to the engineers of EthosEnergy, in order to limit the heat reduction and possibly increase it.

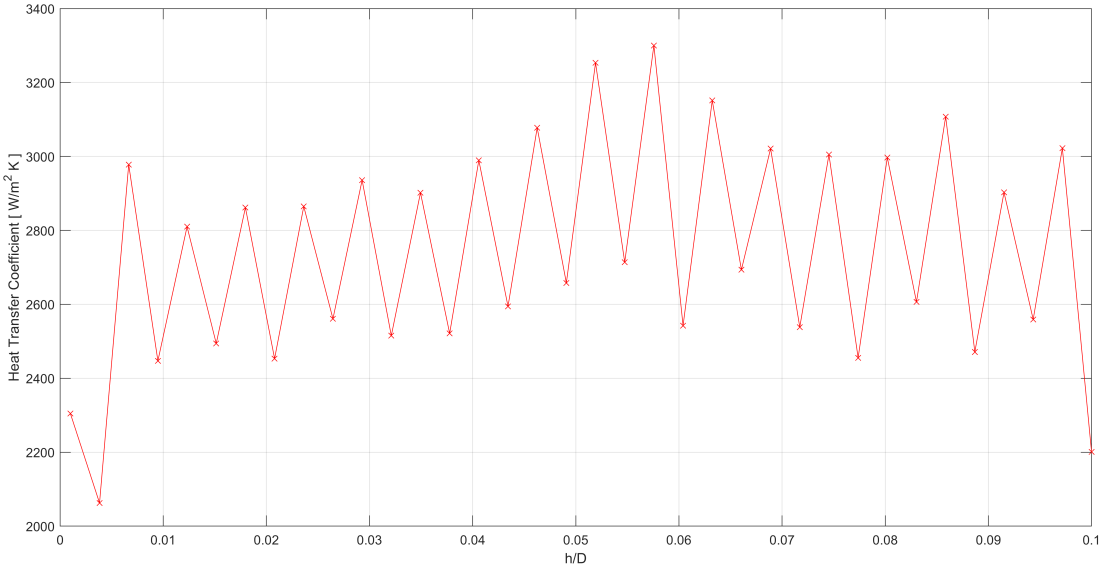

Figure 3.28: Heat Transfer Coefficient - Channel 2

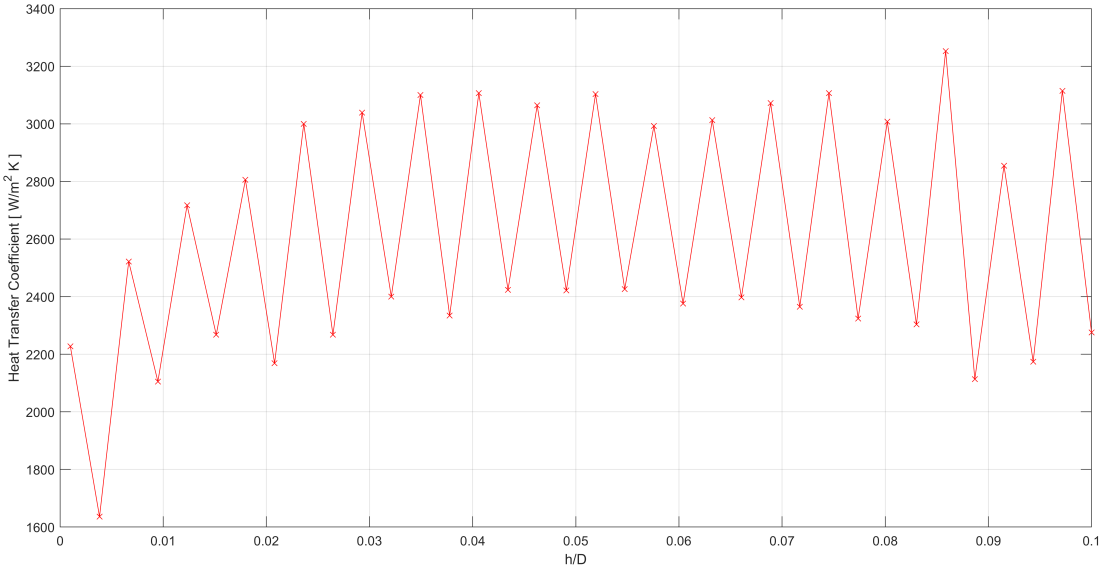

Figure 3.29: Heat Transfer Coefficient - Channel 5

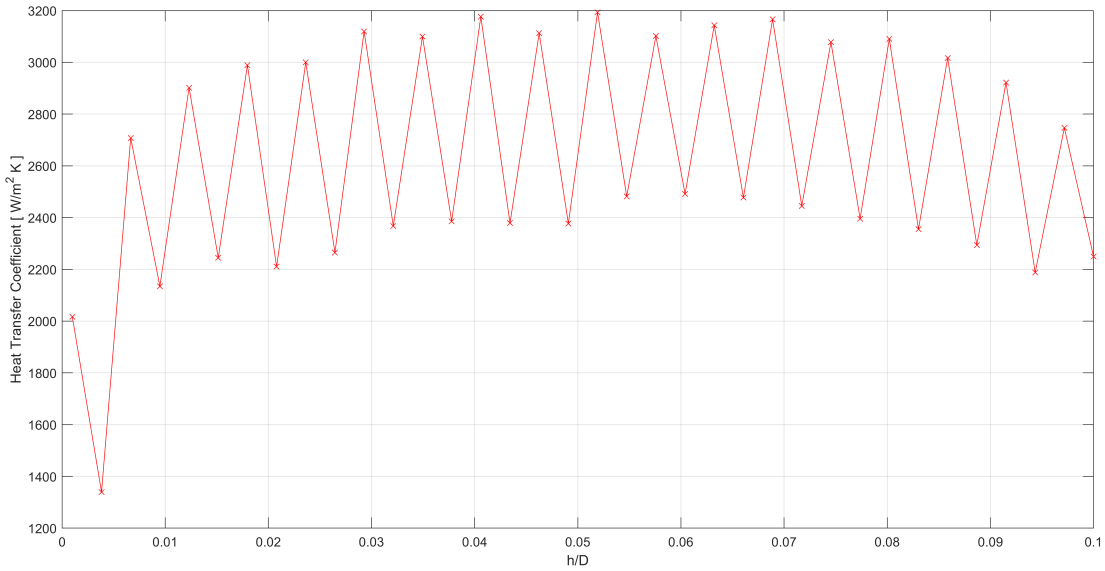

Figure 3.30: Heat Transfer Coefficient - Channel 8

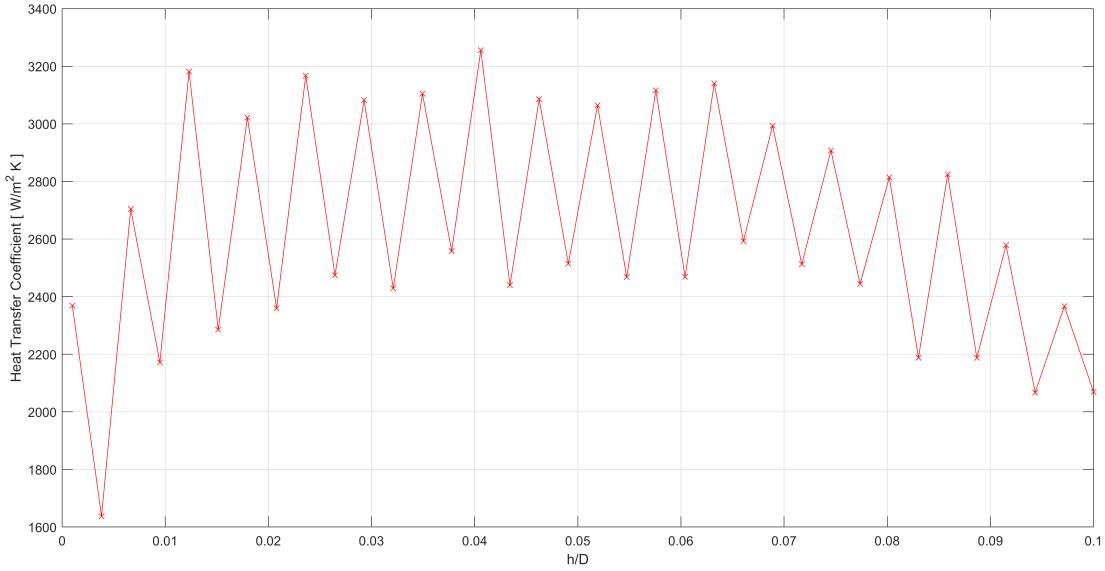

Figure 3.31: Heat Transfer Coefficient - Channel 12

3.7 Case 3: Turbulated channels - Second geometry

The Case 3 represents a new geometry in which the small channels' external diameter has been restored to the original value and the same relative roughness ratio has been applied to the ribs as the first group's channels of the Case 2. Engineers of EthosEnergy wanted to achieve a major reduction in the mass flow rate, despite penalizing the heat transferred from the blade to the coolant.

3.8 Case setup - Case 3

As far as the new geometry is regarded, the same mesh features have been adopted as Case 2 and Case 1.
In this case, since the geometry is different, a little change in the number of cells occurs. For the new turbulated geometry, the total mass flow rate is 15.45 g/s, corresponding to half as Case 1 and 50% more than Case 2. The main drawback of the increased mass flow rate is the reinstatement of the primary stagnation zone in the central region of the core, which was not present in the previous turbulated configuration. Despite this, the secondary stagnation zone disappears allowing for a better distribution of the mass flow rate through the channels of the last group(Fig. 3.32).

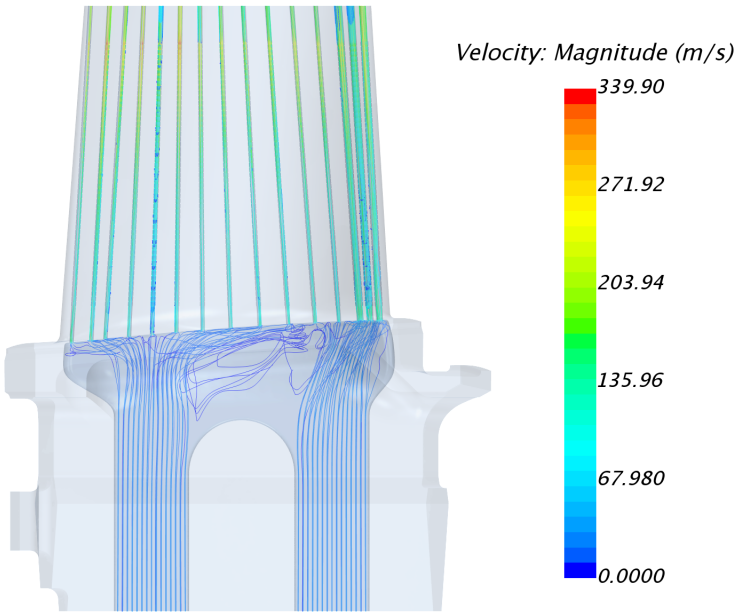

Figure 3.32: Streamlines - Case 3

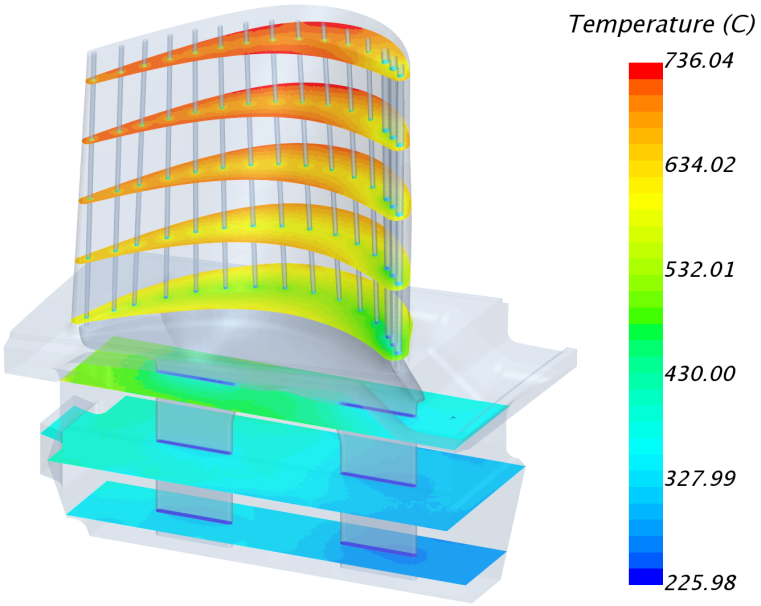

Figure 3.33: Temperature development through the profile - Case 3

Once again, the performance index introduced in Sec. 3.6 to compare the performance of the channels in the smooth and turbulated configuration. By analizing the performance index (Fig. 3.34), it is noticeable that the reduction of the rib height fot the middle channels, has led to a lower advantage between the smooth and turbulated configuration.

Channel #	Smooth MFR [g/s]	Turbulated 2 MFR [g/s]	Smooth Heat Flux [W]	Turbulated 2 Heat Flux [W]	Performance index
1	3.89	2.11	434	371	1.58
2	4.19	2.25	420	365	1.62
3	4.32	2.27	434	381	1.67
4	1.54	0.746	277	206	1.54
5	1.46	0.718	253	185	1.49
6	1.42	0.702	224	163	1.47
7	1.51	0.709	250	184	1.57
8	1.53	0.722	279	209	1.59
9	1.58	0.729	316	229	1.57
10	1.62	0.773	330	243	1.54
11	1.61	0.767	338	243	1.49
12	1.61	0.764	352	251	1.50
13	1.56	0.749	342	241	1.47
14	1.40	0.722	304	217	1.38
15	1.42	0.718	281	184	1.29

Table 3.11: Comparison Case 1 and Case 3

Channel #	Case 2 MFR [g/s]	Case 3 MFR [g/s]	Case 2 Heat Flux [W]	Case 3 Heat Flux [W]	Performance index
1	2.19	2.11	374	371	1.03
2	2.21	2.25	340	365	1.05
3	2.21	2.27	337	381	1.10
4	0.295	0.746	85.7	206	0.95
5	0.295	0.718	100	185	0.762
6	0.295	0.702	109	163	0.628
7	0.305	0.709	118	184	0.67
8	0.305	0.722	120	209	0.736
9	0.305	0.729	121	229	0.792
10	0.316	0.773	125	243	0.795
11	0.314	0.767	122	243	0.815
12	0.314	0.764	125	251	0.825
13	0.308	0.749	112	241	0.885
14	0.304	0.722	106	217	0.862
15	0.305	0.718	92.1	184	0.849

Table 3.12: Comparison between Case 2 and Case 3

Tab. 3.11 shows the comparison of smooth geometry with the second one. Considering that now the channels are characterized by the same ratio e/D, the results for the performance index were expected to be similar for all the channels. It is important to underline the slighlty higher value of the performance index for the first group's channels, with respect to the remaining ones. As a matter of fact, the pitch is the same for all of them, but the ratio p/e is higher for the small channels. An increasing ratio determines an increased heat transfer performance thanks to the different perturbation of the region close to the interface. The variation of the performance index between the channels of the groups from 2 to 4, is, instead, addressed to the non uniform boundary condition and to the asymmetrical distribution of the channels inside the blade.
Tab. 3.12 is the comparison of the Case 2 and Case 3.[1].

[1]The performance index refers to the performance of the Case 3 turbulated channels with respect to the Case 2 turbulated channels

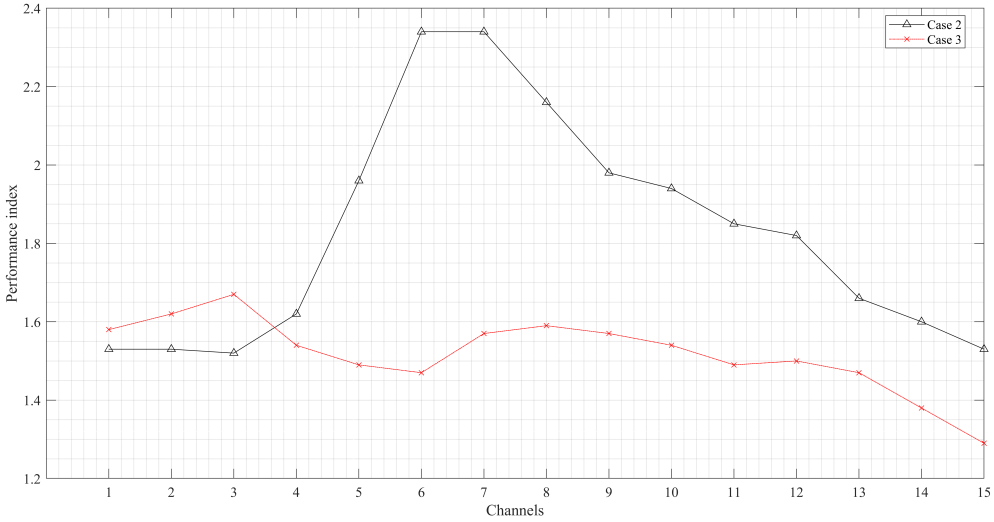

Figure 3.34: Performance index comparison - Case 2 and 3

The analysis of the results for Case 3 (Fig. 3.35, 3.36, 3.37), highlights the more homogeneous distrbution of the mass flow rate in the channels with respect to Case 1. The difference in the pressure drop between channel #14 and the others of the last group is negligible and the same can be said for the mass flow rate.
As far as the boundary heat flux is concerned, the same pattern is present, which is determined by the temperature imposed over the profile. Once again the heat flux is reduced for the channels which experience a lower temperature increase halfway through the blade, and the minimum features the channel #6 as for the smooth channels.

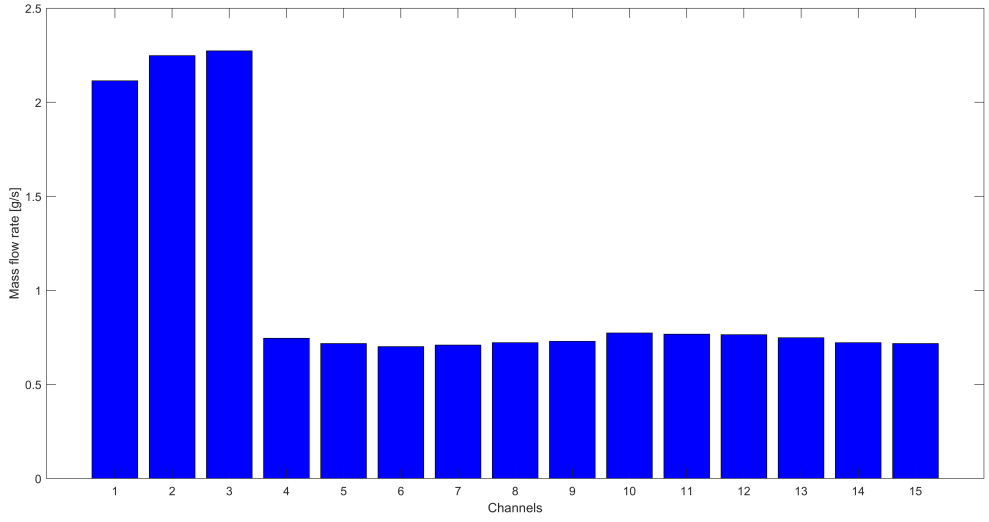

Figure 3.35: Mass flow rates through each channel - Case 3

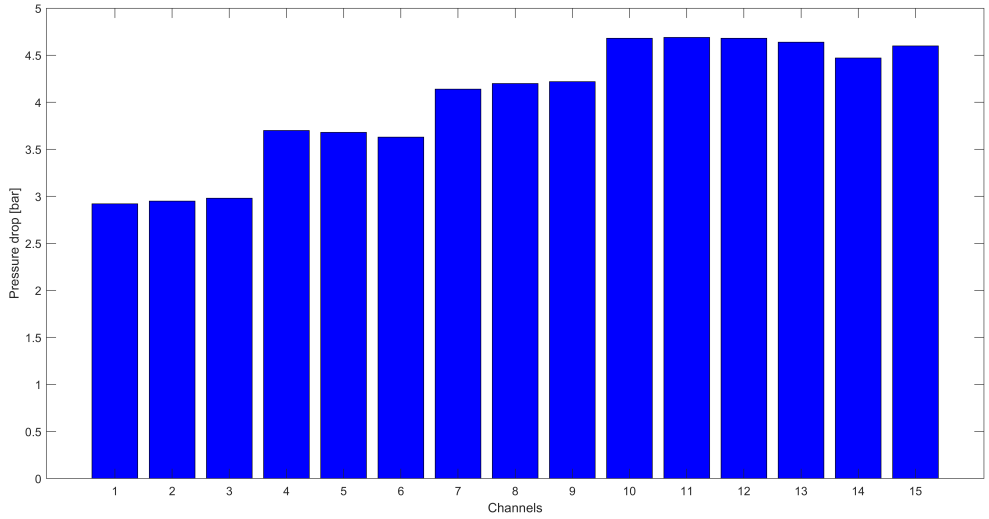

Figure 3.36: Pressure drops through each channel - Case 3

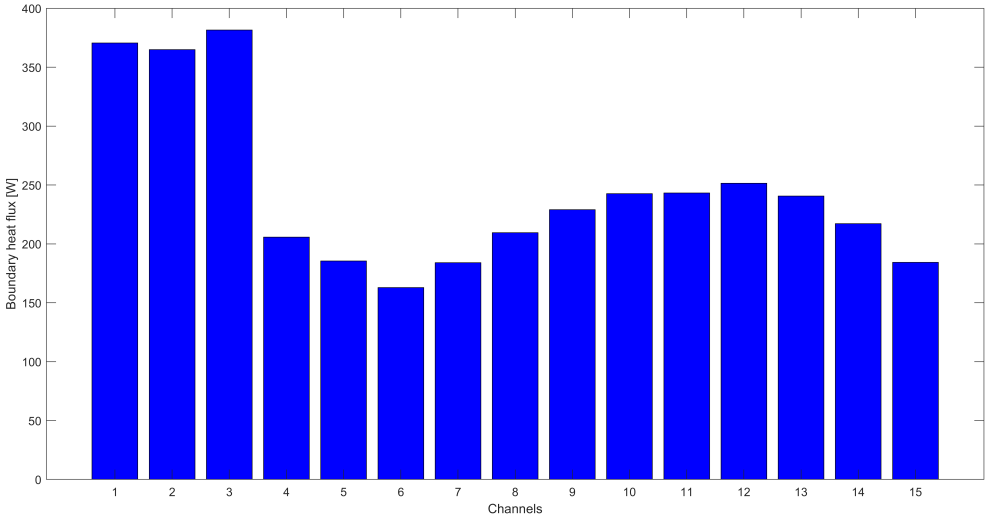

Figure 3.37: Boundary heat flux - Case 3

Fig.3.38 shows the percentage reduction of the mass flow rate through each channel. In order to assess the consistency of these results, the actual dicrease in the mass flow rate for each channel, was compared with the theoretical one coming from the correlations for the friction factors. The comparison is performed according to the following formulation:

$$\frac{MFR_{turb}}{MFR_{smooth}} = \frac{\Delta p_{turb}}{\Delta p_{smooth}} \frac{f_{smooth}}{f_{turb}} \frac{v_{smooth}}{v_{turb}}$$

The predicted reduction in the mass flow rate for the channels of the first group is 50%. As fas as the small channels are regarded, the predicted reduction in te mass flow rate is around 30 %, which is in contrast with the obtained results.

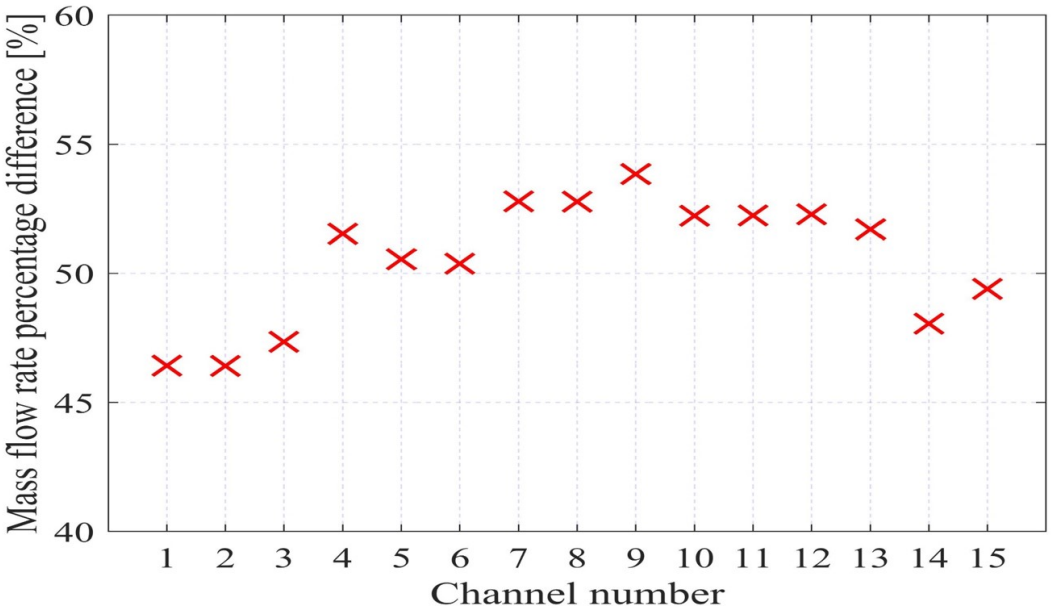

Figure 3.38: Percentage mass reduction through each channel - Case 3

The last part of the section is dedicated to the analysis and comparison of the heat transfer coefficients and the Nusselt number. As we can see from the figures, in correspondence of the ribs, the heat transfer coefficient results to be higher (even by 34 % in the case of Channel #2) with respect to the corresponding smooth channel, thus improving the behaviour of the channel to the heat transfer.
By the comparison of the heat transfer coefficients between Case 2 and Case 3, we can see that channel # 2 features a higher heat transfer coefficient in the entrance region with respect to the Case 2, whereas once the flow develops throght the channel, the difference is unimportant and mainly addressed to numerical instabilities. The reason behind this behaviour is that in the Case 3, the exhausted mass flow rate is a little higher, than the entrance region disturbance determines a higher heat transfer coefficient 3.39.
The same thing can be said as far as the outlet region is concerned. The lower mass flow rate id accompanied by a reduced heat transfer coefficient where the flow pattern tends to stabilize towards a fully-developed regime.
This analysis is carried out only for the channel # 2 since it is the only investigated channel having the same geometrical characteristics in both turbulated setups. It is interesting to show the effect of different fluid-dynamic resistances on the distribution of the flow in the Anima.
For the smooth channels, since the geometry is different, the comparison is meaningful only to assess which geometry performs better, as did previously in the section.

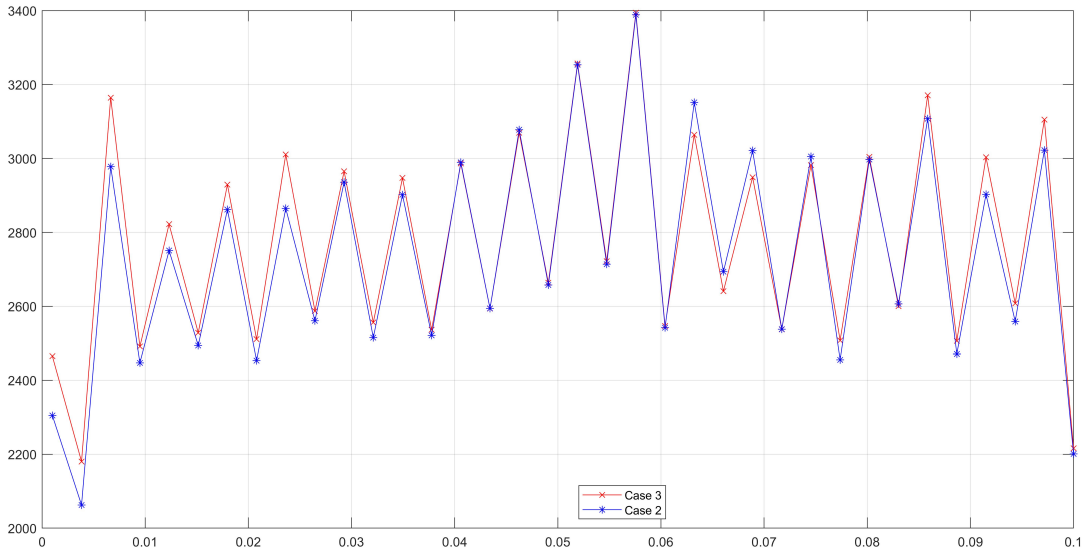

Figure 3.39: Channel 2 - Comparison between Case 2 and 3

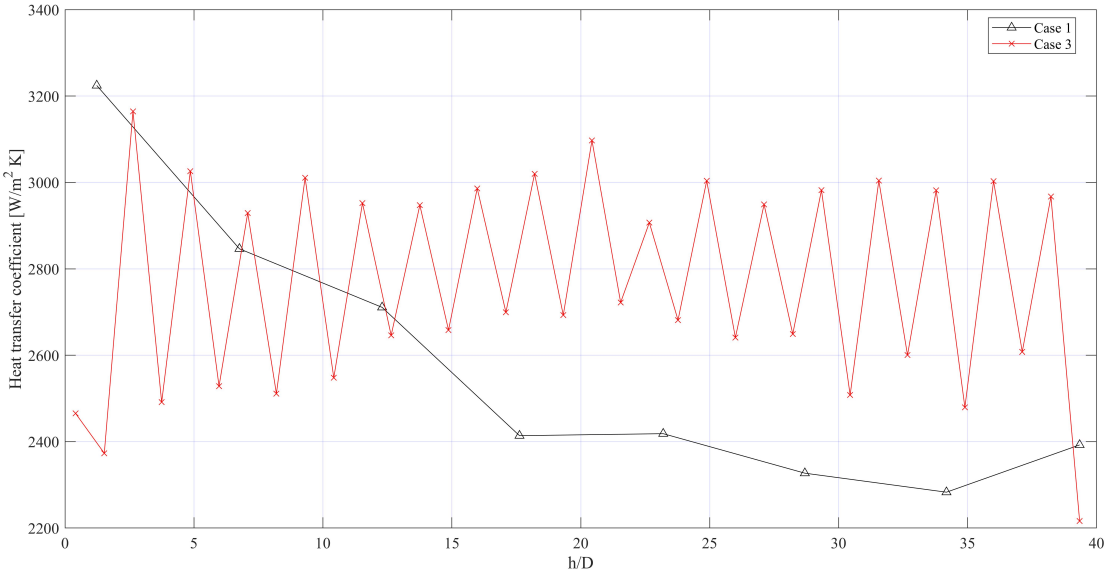

Figure 3.40: Heat transfer coefficient - Channel 2

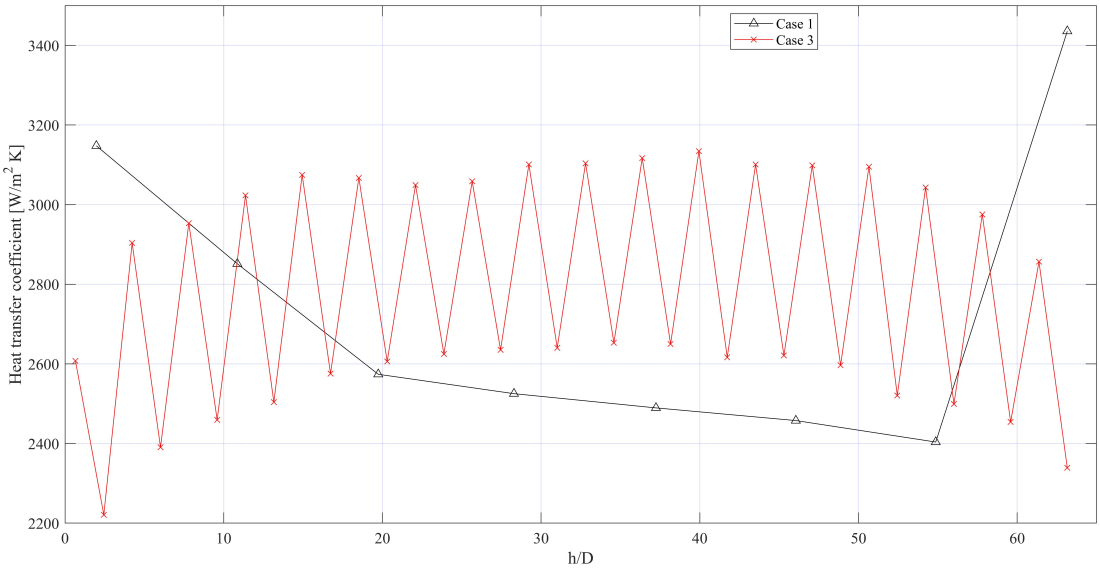

Figure 3.41: Heat transfer coefficient - Channel 5

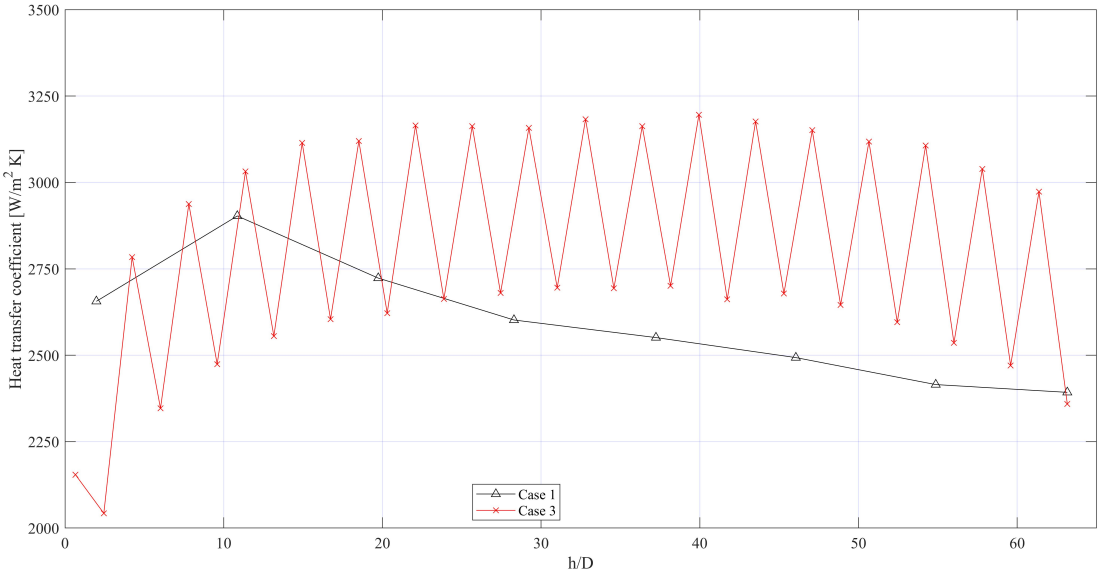

Figure 3.42: Heat transfer coefficient - Channel 8

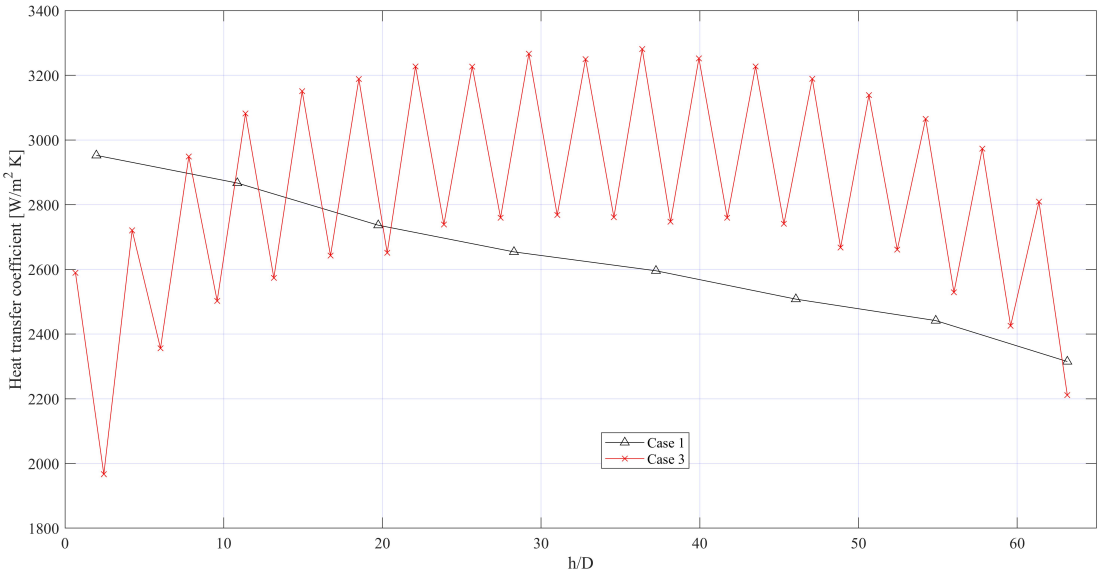

Figure 3.43: Heat transfer coefficient - Channel 12

Chapter 4

Conclusion

In this work, the performance of 3 different geometries of a Turbine Blade were considered. The first case, where stationary smooth channels were adopted was mainly devoted to the effect of the Anima on the fulid-dynamics of the blade.
The main upshot is that for a high mass flow rate feeding the cooling channels, the Anima may have detrimental effects on the distribution of the flow in the expansion region. As a matter of fact 2 stagnation zones came to be, affecting both the heat transfer between the blade and the cooling channels and the distribution of the flow among the channels themselves. This geometry is discouraged eventually.
The second geometry features turbulate cooling channels, whose main characteristics recall an already devised turbine blade. The main effects of turbulation are a better overall performance with respect to the current smooth channels adopted, even tough the target heat exchanged has not been achieved.
In addition, the reduction of the mass flow rate is beneficial, not only for the overall performance of the machine, but even for the redistribution of the flow inside the Anima. As a matter of fact, the lower velocity at the outlet inlet branches, determines the vanishing of the stagnation zones allowing for a better cooling of the blade. The drawback of this geometry is that the mass flow rate is reduced to a too high extent, thus not providing enough coolant for the purpose.
The third investigated geometry is an optimization of the first one, based on the results of the second simulation.
The third geometry once again remarks the overall advantage of a turbulated channel with respect to a smooth one, in a Turbine Blade application. Halfing the total mass flow rate of coolant, a reduction in the heat flux between the channels and the blade of 25 % only has come.

Chapter 5

Next Steps

The main aim of this thesis was to assess the characteristics both in terms of fluid-dynamic and thermal response, of 3 different configuratons of the blade. The CFD has proved to be useful, if not necessary, to evaluate which are the benefits and the drawbacks of each of the configurations, and give some insights in the changes to be adopted in the upcomin future. Despite this, some flaws have to be introduced, in order to give insights about the path to follow to further develope the machine's blade.
First of all, the current thesis has only dealt with one turbulence model, trusting the work currently available in the literature. However, it seems that a shared response about either the chosen model is the best one or not is not found, that's why testing different models with in-house simulations is advised.
The second issue concerns the validation of the results obtained during the simulations for both the single-channel simulation and the full blade. As fas as the single-channel is concerned, a closer look at the flow distribution inside the pipe is necessary. This is helpful for both testing different turbulence models and to compare the flow pattern with the experimental data available in the literature. The distribution of velocities, stagnation zones, flow detachement and so forth can be analyzed, in order to better describe the effect of the ribs on the flow and to correctly predict the effect on the heat transfer coefficient. On the other hand, an experimental analysis of the blade must be performed, to assess the accuracy of the results obtianed through the CFD simulation.
This is of main importance to make sure that the performance's forecasts are correct and the machine can work in the proper way through the new design.
As highlighted through the simulation with the radial Temperature profile, the distribution of the Temperature highly affects the flow distribution and heat transfer coefficient in the channels. For this reason, despite the FEM analysis has been reassuring about the almost-independence of the temperature distribution from the internal cooling, a conjugate analysis in which the primary air flow is simulated could be performed. As a matter of fact, we must remember that ANSYS takes as an input the heat transfer coefficients for

the external flow, which are computed through a similitude approach, and the solutions from the Mean-Line analysis have not been implemented yet.
Eventually, extending the simulations to different rib pitches and heights, a trend for the mass flow rate and heat flux can be drawn to furtherly optimize the geometry, in accordance with technological limitations.

Nomenclature

β_k compression ratio
γ heat capacities ratio
ϵ rate of dissipation of turbulence energy
ϵ_r relative error
η turbulated channels efficiency index
η_{id} ideal cycle efficiency
η_t isoentropic efficiency of the turbine
η_k isoentropic efficiency of the compressor
μ dynamic viscosity
μ_T turbulent viscosity
k turbulence specific kinetic energy
ρ density
ρ_T density derivative with respect to temperature
Π_ν viscous stress tensor
w dissipation per unit turbulence kinetic energy

a acceleration
c_p specific heat at constant pressure
c_v specifi heat at constant volume
D external diameter of the pipe
DNS direct numerical simulation
e rib height
e specific energy
e_t total specific energy
f friction factor
h specific enthalpy
f_{exact} exact solution
F_s safety factor
GCI grid convergence index
h heat transfer coefficient

k thermal conductivity
L pipe length
LE leading edge
LES large eddy simulation
$\dot{m}_f$ mass flow rate
$\dot{m}_f\prime$ mass flow rate correction
MFR_{char} characteristic mass flow rate of a nozzle
Nu Nusselt's number
p rib pitch
p_{in} inlet pressure
p_{std} standard pressure
P pumping power
Pe Peclet number
Pr Prandtl's number
PS pressure side
$\mathbf{q}_\alpha$ specific thermal heat flux
Q specific heat
R gas constant
Re Reynold's number
SS suction side
St Stanton's number
T_{env} environmental temperature
T_b bulk temperature
T_{in} inlet temperature
T_{std} standard temperature
T_w wall temperature
TE trailing edge
TIT turbine inlet temperature
$\mathbf{u}$ velocity
U_r^2 reference velocity
$\mathbf{x}$ position vector

$\frac{e}{D}$ relative roughness
$\frac{p}{e}$ relative spacing

Bibliography

[1] B. Lakshminarayana, *Fluid Dynamics and Heat transfer of Turbomachinery*, Copyright Wiley-VCH Verlag GmbH & Co. KGaA.

[2] J.C. Han, S. Dutta and S. Ekkad, *Gas Turbine Heat Transfer and Cooling Technology*, Taylor and Francis, New York, NY,USA,2000

[3] Luai M. Al-Hadhrami, S.M. Shaahid and Ali A. Al-Mubarak, Jet Impingement Cooling in Gas Turbines for Improving Thermal Efficiency and Power Density, Saudi Arabia

[4] D.C. Wilcox, *Turbulence Modeling for CFD (3rd edition)*, DWC Industries, 2006

[5] H. K. Versteeg, W. Malalasekera *An Introduction to Computational Fluid-Dynamics - The Finite Volume Method (2nd edition)*, Pearson Education ,2007

[6] P.J. Roache *Perspective: A method for Uniform Reporting of Grid Refinement Studies*, 1994

[7] U. Trottenberg; C. W. Oosterlee; A. Schüller,
textitMultigrid, Academic Press, 2001

[8] R.L. Webb, E.R.G. Eckert, R.J. Goldstein, *Generalized heat transfer and friction correlations for tubes with repeated-rib roughness*,Int.J. Heat Mass Transfer, 1971

[9] A. Riggio, *Thermal-Structural FEM analyses of upgraded components of an industrial gas turbine*, 2019

[10] F. Cardile, *CFD Analysis of the Cooling Flow in a Heavy Industrial Gas Turbine Blade*,2019

[11] S. d'Imperio, *Steady-state turbogas plant performance optimization through mean-line and stream-line analysis of turbine and compressor*, 2019

List of Figures

List of Tables